Regulation of Eag by calcium/calmodulin controls presynaptic excitability in *Drosophila*

Running title: Eag's CaMBD regulates excitability

Peter Bronk, Elena A. Kuklin, Chang Liu, Timothy D. Wiggin, Srinivas Gorur-Shandilya, Eve Marder and Leslie C. Griffith*

Department of Biology, National Center for Behavioral Genomics and Volen Center for Complex Systems, Brandeis University, Waltham, MA, 02454-9110 USA

***Correspondence:**

Leslie C. Griffith
Brandeis University
Department of Biology MS008
415 South Street,
Waltham, MA, 02454-9110, USA
Tel: 781 736 3125
griffith@brandeis.edu

Acknowledgements

We would like to thank Rob Reenan (Brown University) for generously sharing *eag* constructs and for his advice on techniques for homologous recombination, and Ed Dougherty for assistance with confocal imaging.

Grants

This work was funded by R01 GM54408 to LCG, R35 NS097343 (to EM) and F32 NS098624 (to TDW).
.

Disclosures

The authors declare no competing financial interests

Author Contributions

PB and LCG conceived and designed the experiments. PB created mutants, performed all biochemical and electrophysiology experiments and analyzed the data. CL assayed sleep and memory and analyzed behavioral data. EAK performed morphological analyses of the NMJ. SGS and EM conceptualized and built the model. TDW performed and analyzed the imaging experiments. PB and LCG wrote the paper with editing from the other authors.

Abstract

Drosophila ether-à-go-go (eag) is the founding member of a large family of voltage-gated potassium channels, the KCNH family, which includes Kv10, 11 and 12, (Ganetzky et al. 1999). Mammalian EAG1 channels are inhibited by binding of calcium/calmodulin (Ca^{+2}/CaM) at sub-micromolar Ca^{2+} concentrations (Schonherr et al. 2000) as a result of the concurrent binding of Ca^{2+}/CaM to N- and C-terminal sites causing pore constriction (Whicher and MacKinnon 2016). Although the *Drosophila* EAG channel was believed to be Ca^{2+}-insensitive (Schonherr et al. 2000), both the N- and C-terminal sites are conserved. Here we show that *Drosophila* EAG is inhibited by high Ca^{2+} concentrations that are likely only present at plasma membrane Ca^{2+} channel microdomains. To test the role of this regulation *in vivo*, we engineered mutations that block CaM-binding to the major C-terminal site of the endogenous *eag* locus, disrupting Ca^{2+}-dependent gating. *eag* CaMBD mutants have reduced evoked release from larval motor neuron presynaptic terminals and show decreased Ca^{2+} influx in stimulated adult projection neuron presynaptic terminals. These results are consistent with a conductance-based multi-compartment model of the presynaptic terminal. The reduction of release in the larval neuromuscular junction drives a homeostatic increase in motor neuron somatic excitability. This misregulation of synaptic and somatic excitability has consequences for systems-level processes and leads to defects in associative memory formation in adults.

Significance Statement

Regulation of excitability is critical to tuning the nervous system for complex behaviors. We demonstrate here that the EAG family of voltage-gated potassium channel exhibits conserved gating by Ca^{2+}/CaM. Disruption of this regulation in *Drosophila* results in a decrease in evoked neurotransmitter release due to truncated Ca^{2+} influx in presynaptic terminals. In the larval motor system the blunting of evoked responses triggers a homeostatic increase in somatic excitability, which would act to compensate for the decrease in muscle stimulation. In adults, disrupted Ca^{2+} dynamics lead to defects in memory formation. These data demonstrate that the biophysical details of channels can have widespread effects on behavior at the level of cellular compartments and circuits.

Introduction

The repolarization of neurons and muscle cells by potassium channels plays an important role in limiting the excitability of cells and returning them to a baseline membrane potential to be ready for the next action potential. Potassium channels also play an indirect role in regulating Ca^{2+} levels inside the cell, preventing excitotoxicity and shaping the temporal profile of cellular responses to activity. Several families of Ca^{2+}-activated potassium channels (e.g. small and large conductance, SK and BK channels), appear to act in a feedback mode, with internal Ca^{2+} activating the channels to hyperpolarize the cell and limit additional Ca^{2+} entry. However, there is one Ca^{2+}-regulated potassium channel family that appears to act in a counterintuitive manner. The mammalian Ether-à-go-go (EAG) potassium channel is completely inhibited at all membrane voltages in the presence of 100-300 nM Ca^{2+}/calmodulin (Ca^{2+}/CaM; Schonherr et al. 2000; Stansfeld et al. 1996; Whicher and MacKinnon 2016; Ziechner et al. 2006). We sought to understand the role of this seemingly maladaptive regulation by disrupting the CaM interaction with EAG in *Drosophila* where the presence of only one gene coding for EAG simplifies the analysis.

The *Drosophila ether-à-go-go* (*eag*) gene encodes a voltage-gated delayed rectifier potassium channel subunit, EAG. The first *eag* mutant was discovered in *Drosophila* and was identified by its ether-induced leg shaking (Kaplan 1969). Subsequently, *Drosophila* EAG was found to define a family of potassium channels with multiple homologs in mammals (Warmke and Ganetzky 1994). EAG is a member of the KCNH family of potassium channels and is also referred to as Kv10 (Gutman et al. 2003). Although the transmembrane domains of EAG are similar in structure to Shaker-type voltage-gated channels (Warmke and Ganetzky 1994), recent structural data has shown that EAG has a novel gating mechanism. This alternate gating mechanism allows cytoplasmic factors like CaM to act on the pore region through the domain linking the C-terminus to the S6 transmembrane domain (Whicher and MacKinnon 2016). Channel closure is achieved by the simultaneous binding of Ca^{2+}/CaM to both an N-terminal and a C-terminal site. This requirement for binding at two sites means that disruption of a single CaM binding domain (CaMBD) blocks Ca^{2+}-dependent gating entirely (Schonherr et al. 2000).

The biophysical properties of EAG have been determined in heterologous expression systems, and little is known about its function in the nervous system. Fly loss of function *eag* mutants have learning deficits (Griffith et al. 1994) in addition to a robust hyperexcitability in larval motor neurons that also causes spontaneous neuronal firing (Drysdale et al. 1991b; Ganetzky and Wu 1983; Griffith et al. 1994; Srinivasan et al. 2012). EAG1 knock-out mice have normal learning and memory, sensorimotor function, social behavior, anxiety and only display a

128 mild hyperactivity (Ufartes et al. 2013). However, the existence of multiple EAG family members
129 in mammals raises the possibility of compensation or redundancy and complicates *in vivo*
130 analysis. Cellular physiology in EAG1 knock-out mice has revealed enhanced synaptic
131 facilitation during high frequency stimulation (>= 50 Hz) at the parallel fiber-Purkinje cell
132 synapse in the cerebellum, accompanied by elevated presynaptic Ca^{2+} (Mortensen et al. 2015).
133 In both insects and mammals, the dominant phenotype of loss of EAG channels appears to be
134 increased presynaptic release.
135 The role of gating by Ca^{2+}/CaM *in vivo* is likely to be more complicated, and
136 understanding the role of Ca^{2+} inhibition requires generating an EAG channel that is voltage-
137 gated, but lacks Ca^{2+}/CaM inhibition. In this study we show that fly EAG is inhibited by
138 Ca^{2+}/CaM, and we generate mutant alleles disrupting the CaM interaction with EAG to
139 interrogate its function. We find that without Ca^{2+}/CaM inhibition of EAG, evoked synaptic
140 currents are reduced, and presynaptic Ca^{2+} is reduced during high frequency stimulation. These
141 defects lead to homeostatic changes in somatic excitability that go in the opposite direction. The
142 complex misregulation of excitability in these mutants disrupts higher level behavior,
143 demonstrating that the biophysical details of channel regulation can have profound effects at the
144 organismal level.
145
146 **Materials and Methods**
147 ***Drosophila* crosses for recording and protein analysis**
148 Crosses to produce larvae for electrophysiology were set up in vials with 5-6 females and 5
149 males for each genotype to have consistent numbers of larvae between genotypes and kept at
150 around 22° C in the lab. Crosses were flipped every 3-5 days, but no more than 4 times. Bottle
151 crosses were used for protein extraction. The single alleles analyzed were hemizygous males
152 resulting from a cross of homozygous control or CaMBD mutant females to *w* males. The
153 transheterozygous alleles were females resulting from crossing 2 homozygous alleles of control
154 (WT12 and WT8) or CaMBD mutants (CaMBD8 and CaMBD17). Whenever possible the
155 transheterozygous combinations were used to reduce the effect of potential off target mutations
156 not eliminated during outcrossing of stocks.
157
158 **Generation of mutant strains**
159 Control and Calmodulin binding domain (CaMBD) mutant knock-in strains were generated by
160 targeted ends-out homologous recombination using methods described in detail previously
161 (Staber et al. 2011). The homologous arms were amplified by PCR from genomic DNA and

162 each arm was cloned into a Topo vector and were a kind gift from the laboratory of Robert
163 Reenan at Brown University. Mutations to the arm spanning the C2 CaMBD were made by site
164 directed mutagenesis using primers
165 CGTCCGGAAGATATCCTCCAAATCTCGTCGCACTCCGC (forward) and
166 GCGGAGTGCGACGAGATTTGGAGGATATCTTCCGGACG (reverse). The arms were cloned
167 sequentially into a P[w25.2] target vector. The full *eag* deletion mutant was generated using
168 piggyBack insertions containing FRT sites (Thibault et al. 2004) as described previously (Parks
169 et al. 2004). Briefly, Exelixis stocks PBac{RB}e03618 and PBac{WH}f02960 (p-element on X
170 chromosome) were used to delete the entire *eag* gene. PBac{RB}e03618/FM7a flies were
171 crossed to hs-FLP/Bal and male progeny were crossed to PBac{WH}f02960 females. After 48
172 hours, the bottle crosses were heat shocked in a 37º C water bath for 1 hour to activate the FLP
173 recombinase. The parents were removed after 72 hours and the bottles were heat shocked daily
174 (1 hour at 37º C) for 4 more days. The candidate flies were balanced and screened by PCR
175 using paired element-specific and genome-specific primers:
176 PB08014: GATCATTAAAACGTGGCCAACTAC (5' *eag* flanking region e03618)
177 PB08013: CCTCGATATACAGACCGATAAAAC (element specific primer)
178 PB08015: GTGGGGGTTCTTATTCTTCAGTT (3' eag flanking region f02960).
179
180 **Electrophysiology**
181 *Solutions: Nominally Ca^{2+}-free HL3.1* (Feng et al. 2004) (in mM): 70 NaCl, 5 KCl, 4
182 $MgCl_2$, 10 $NaHCO_3$, 5 Trehalose, 115 sucrose, 5 HEPES; pH adjusted to 7.1-7.2 with NaOH. *0*
183 *Ca^{2+} Modified A solution* (in mM): NaCl, 118; KCl, 2; $MgCl_2$, 4; Trehalose, 5; Sucrose, 45.5;
184 HEPES, 5; EGTA, 0.5; pH adjusted to pH 7.3-7.4 with NaOH. *Nominally Ca^{2+}-free Modified A*
185 *solution* (in mM): NaCl, 118; KCl, 2; $MgCl_2$, 4; Trehalose, 5; Sucrose, 45.5; HEPES, 5; pH
186 adjusted to pH 7.3-7.4 with NaOH. *HEK cell low Ca^{2+} internal patch solution* (in mM): NaCl, 2; K-
187 Gluconate, 130; $CaCl_2$, 0.1; $MgCl_2$, 2; EGTA, 1; HEPES, 10; pH adjusted to 7.3-7.4 with KOH.
188 *Motor neuron low Ca^{2+} internal patch solution* (in mM): 2 NaCl, 130 K-Gluconate, 0.1 $CaCl_2$, 1
189 EGTA, 0.5 Na-GTP, 4 Mg-ATP, 10 HEPES) adjusted to 285 mOsm with glucose, and pH 7.3-
190 7.4 with KOH.
191 HEK cell recordings by whole-cell patch were made 48 to 60 hours after transfection.
192 Cells were recorded at 21-22° C in 0 Ca^{2+} modified A solution (see solutions section) and a low
193 Ca^{2+} internal patch solution (see above). The appropriate amount of Ca^{2+} was added to the
194 internal solution to yield the approximate calculated free Ca^{2+} concentrations shown in the
195 figure. The Maxchelator program (Chris Patton, Stanford University) was used to calculate the

196 free Ca^{2+} concentrations. The HEK cells were voltage clamped with a Multiclamp 700A amplifier
197 (Axon Instruments, Molecular Devices, Sunnyvale, CA) and currents were filtered at 2.6 kHz
198 and recorded using pClamp 8 software (Axon Instruments, Molecular Devices). Software
199 sampling at 10 kHz. Leak currents were calculated offline by fitting the steady state current vs.
200 voltage relationship from -80 mV to -60 mV. The slope and intercept of the linear fit was used to
201 calculate the leak current at each membrane potential and subtracted from the recorded
202 sustained currents. EAG transfected cells were rejected if the initial resting potential was < 20
203 mV. The recording for the different EAG isoforms (Figure 1E) were performed as above except
204 that the internal pipette solution was changed to increase EGTA to 5 mM and 4 mM Mg-ATP
205 was added.
206 Potentials from the neuromuscular junction (NMJ) were recorded in current clamp mode
207 from muscle 6 of wandering third instar (gender specified in fly cross methods) larvae with
208 intracellular electrodes filled with 3 M KCl (20-30 MΩ) in 0.4 mM or 0.2 mM Ca^{2+} HL3.1. Signals
209 were amplified with an Axoclamp 2B amplifier (Molecular Devices, Sunnyvale, CA), digitized
210 with a Digidata 1322A (Molecular Devices), and recorded at 10 kHz with pClamp8 software
211 (Molecular Devices). Muscles with resting potentials more depolarized than -45 mV were not
212 used. The mEJP and nerve evoked recordings were done in 0.2 mM Ca^{2+} HL3.1 except with 2
213 mM KCl to increase the potassium driving force. The motor nerves were stimulated with a glass
214 pipette ~10 μm in diameter at 2-3 times the threshold voltage to first trigger a postsynaptic
215 response.
216 Synaptic currents at the NMJ were recorded from larval muscle 6 of wandering 3rd instar
217 larvae in two-electrode voltage clamp (TEVC) mode with an Axoclamp 2B amplifier and digitized
218 as above. We used 0.2 mM Ca^{2+} HL3.1 solution except that the KCl was adjusted to 2 mM. The
219 3 M KCl filled voltage sensing electrodes had resistances of 15-18 MΩ, and the current passing
220 electrodes filled with 3 M KCl had resistances of 10-15 MΩ. The muscles were held at -70 mV.
221 Cells were rejected if, after impaling the muscle with both electrodes, the average of the 2
222 resting potentials recorded at each electrode was more depolarized than -30 mV.
223 Type Is motor neuron voltages were recorded by whole-cell patch clamp in current
224 clamp mode with a Multiclamp 700A amplifier (Molecular Devices, Sunnyvale, CA). Filtering and
225 sampling as for HEK cells. Larvae were filleted in Ca^{2+}-free modified A solution and the brain left
226 intact. Dorsal motor neurons directly below the sheath of the ventral nerve cord were visualized
227 with a 40x water immersion objective and exposed by applying 0.2 % w/v protease (type XIV,
228 MilliporeSigma, St. Louis, MO) in Ca^{2+}-free modified A solution with a patch pipette directly
229 around the cluster of neurons. The patch pipettes for recording had resistances of 2-3 MΩ

230 containing internal solution (see solutions section). Recordings were made first in nominally
231 Ca^{2+}-free modified A solution and then the solution was changed to a 1.8 mM Ca^{2+} modified A
232 solution. Current was injected to keep the motor neurons at -60 mV. Cells were rejected if the
233 initial resting potential was more depolarized than -40 mV, or if the initial access resistance
234 exceeded 50 MΩ.
235 All physiological preparations were superfused with the indicated saline solutions by
236 gravity feed and vacuum suction at 1-2 ml/min. Electrophysiology trace plotting and analysis of
237 membrane current and voltage signals were performed in MATLAB (Mathworks, Natick, MA)
238 using scripts written by PB. Table 1. shows cell properties recorded for each of the data sets in
239 this study.
240
241 **Protein analysis**
242 For immunoblots, HEK cells were washed 2x with 1x PBS and then cells were scraped
243 in 500 μl 2x Laemmli sample buffer. The cell suspension was passed through a syringe needle
244 2-3x to break up the membranes. The homogenate was separated by 7.5% SDS-PAGE, and
245 immunoblotted with an anti-Eag rabbit polyclonal antibody raised against amino acids 1032-
246 1174 of *Drosophila* Eag.
247 For CaM-agarose purification of EAG, 1 ml of flies of each genotype were collected in a
248 15 ml conical centrifuge tube and frozen on dry ice. The frozen flies were vortexed and dumped
249 onto a sieve to collect the heads that pass through on a fine mesh cooled on dry ice. The heads
250 were put into 1.5 ml eppendorph tubes on dry ice, and then transferred to a Dounce
251 homogenizer (2 ml) on ice. 100 ml of homogenization solution (20 mM HEPES-NaOH pH 7.4, 1
252 mM EGTA) was added and the heads were homogenized. The homogenate was transferred to
253 a fresh 1.5 ml eppendorph tube and 100 ml additional homogenization solution was added to
254 the homogenizer to wash and collect the remaining homogenate. 200 ml of 2x solubilization
255 buffer (20 mM HEPES-NaOH pH 7.4, 200 mM NaCl, 2% Triton X-100, 1 mM EGTA) was added
256 to the homogenate. Both buffers contained a broad spectrum protease inhibitor, Complete Mini
257 (Roche Diagnostics, Germany). The tubes of homogenate were rotated at 4° C for 1 hour and
258 centrifuged for 15 minutes (4° C, 14,000 rpm). The supernatant was added to 100 μl of
259 sepharose beads conjugated to Calmodulin (equilibrated in same buffers used in solubilization
260 step) along with Ca^{2+} to a final concentration of 2 mM and rotated 1 hour at 4° C. 100 μl of the
261 supernatant (flow through) was removed from each sample before washing the beads in Ca^{2+}
262 containing buffer 3x. 100 μl of 2x Laemmli sample buffer was added to the beads and then the
263 samples were boiled for 10 min. Samples were separated by 7.5% SDS-PAGE, and

264 immunoblotted with an anti-Eag rabbit polyclonal antibody (1:500) raised against amino acids
265 1032-1174 of *Drosophila* Eag, and Actin antibody, 1:5000 (EMD Millipore).
266
267 **Immunohistochemistry**
268 *Larval brain:* Wandering 3rd instar larvae were filleted and pinned out in Sylgard coated
269 35 x 15 mm petri dishes (3 larvae/dish) containing ice cold Ca^{2+}-free HL3.1 solution. The HL3.1
270 solution was removed and replaced by fresh ice cold 4% paraformaldehyde in PBS and
271 incubated at 4° C on an orbital shaker for 4 hours. Fixed preparations were washed 3 x 5
272 minutes with PBS-TX (0.2% Triton-X-100 in PBS) and then blocked overnight at 4° C in PBS-
273 TX-BSA (0.2% Triton-X-100 and 5% bovine serum albumin in PBS). The head and first few
274 abdominal segments were cut from the rest of the larval body (with the brain attached) and
275 placed into wells of a 60 well minitray (Nunc, Denmark) (1 larva/well) containing rabbit EAG
276 antibody (1:500) in PBS-TX-BSA and mouse Actin antibody, 1:1500 (EMD Millipore) in PBS-TX-
277 BSA. The tissue was incubated at room temperature for 2 hours on an orbital shaker and
278 washed 3 x 5 minutes with PBS-TX. 1:200 Alexa Fluor 488 goat anti-rabbit (Invitrogen,
279 Molecular Probes) and 1:200 Alexa Fluor 680 goat anti-mouse (Invitrogen, Molecular Probes) in
280 PBS-TX-BSA were added to the well and incubated at room temperature for 1.5 to 2 hours. The
281 brain preparations were then washed 3 x 5 minutes and mounted on slides in Vectashield
282 (Vector Laboratories, Burlingame, CA) still attached to the head to keep the brain oriented.
283 Sequential images of the green and red emission signals were taken using the 63x objective on
284 a Leica TCS SP2 confocal microscope. Ten optical sections (1.2 μm each) were taken for each
285 brain using identical settings making sure none of the signals were saturated. The pixel
286 intensities were analyzed using MATLAB (Mathworks, Natick, MA) by averaging the pixel
287 intensity in the same region of the neuropil for each optical section and subtracting the average
288 pixel intensity in the background. The ratio of Green:Red pixel intensities was calculated for
289 each brain.
290 *Larval NMJ:* Wandering 3rd instar larvae were filleted and pinned out in Sylgard coated
291 35 x 15 mm petri dishes containing ice cold Ca^{2+}-free HL3.1 solution. The motor nerves were
292 cut carefully and the brain was removed before replacing the solution with ice cold 4%
293 paraformaldehyde in PBS and incubating at room temperature on an orbital shaker for 20
294 minutes. After a quick rinse in PBS, the prep was washed in PBS for 20 minutes at room
295 temperature on an orbital shaker. Then the larval preparations were washed 3 x 10 minutes at
296 room temperature in PBT (PBS + 0.05% Triton X-100). The larval tissue was then blocked for 1
297 hour at room temperature in blocking solution (5% heat inactivated goat serum + PBT). Mouse

298 4F3 anti-DLG antibody (Developmental Studies Hybridoma Bank) was diluted 1:50 in blocking
299 solution and added to the larval preparations and they were incubated overnight at 4º C on an
300 orbital shaker. After 3 x 10 minute washes in PBT, the larval preparations were incubated with
301 goat anti-mouse Alexa-Fluor 488 (Invitrogen) diluted 1:200 in PBS and Alexa-Fluor 594-
302 conjugated goat anti-HRP (1:200, Jackson ImmunoResearch Laboratories) for 2-3 hours at
303 room temperature. Final washes in PBT (5 x 5 minutes). The larval preparations were then
304 mounted on slides in Vectashield (Vector Laboratories, Burlingame, CA). Images of the NMJs
305 were taken sequentially at the appropriate emission spectra on a Leica TCS SP5 confocal
306 microscope. Only boutons associated with DLG staining were counted from muscles 6/7 in
307 segments A2 or A3.
308
309 **Cell culture and plasmids**
310 HEK cells were grown in DMEM (Gibco/Life Technologies) supplemented with heat inactivated
311 bovine serum (Invitrogen). Cells were transfected with EAG plasmids (4 μg/100 mm plate) using
312 the Ca^{2+}-phosphate method, and co-transfected with GFP (1 μg/100 mm plate). After 6 hours,
313 transfected cells were resuspended and plated onto 35 mm plates coated with poly-L-lysine. 24
314 hours after transfection, cells were transferred to a 26° C incubator. This was necessary for the
315 expression of functional *Drosophila* Eag channels in HEK cells (Li et al. 2011). HEK cells were
316 transfected with a pcDNA3 vector backbone containing wild type or mutant *eag* cDNA (PA). The
317 C2 CaM binding domain mutations, F232S,F235S were generated by site-directed mutagenesis
318 (Stratagene) using primers: CGTCCGGAAGATATCCTCCAAATCTCGTCGCACTCCGC
319 (forward) and GCGGAGTGCGACGAGATTTGGAGGATATCTTCCGGACG (reverse). The
320 correct sequence of the plasmids was verified over the entire length of the cDNA. The splice
321 isoforms EAG-PE and EAG-PF were constructed from the EAG-PA plasmid described above
322 with the Gibson cloning method using 5 primers:
323 F10: GACTCACTATAGGGAGACCCAAGCTTGGTACCGAGCTCGGATCC
324 R11: GCCAATTTGGCGAATTTCGAGAGACCTCCCTTCGTGTCCTCGCTGTCG
325 R14:GCGAATTTCGAGAGACCAGGGAGAAACAGGTTGACGGCAAAACTCCCTTCGTGTCCT
326 CG
327 F12: GTCTCTCGAAATTCGCCAAATTGGCAAGATCAGTGACACG
328 R13: TTCTCGTTGTCTGTCTCCGCGGCGACATTGCCAAAGCCCACC
329 3 PCR reactions were performed. PCR a- F10:R11, PCR b- F10:R14, PCR c- F12:R13. Region
330 of editing was checked by sequencing.
331

332 **Calcium Imaging of Adult *Drosophila* Neurons**

333 Homozygous *eag* CaMBD17 mutant and *eag* WT12 control female flies were crossed
334 with transgenic flies carrying *GH146-GAL4* (Bloomington Stock # 30026) and *UAS-GCaMP6f*
335 (Bloomington Stock # 52869). Male progeny were screened for transgene expression by eye
336 color and housed at 25°C for 5-10 days post eclosion. Experimental animals were anesthetized
337 with ice, and brains were dissected in Adult Hemolymph-Like (AHL) saline (Wang et al. 2003).
338 *Ex vivo* brains were secured to a Sylgard-lined perfusion chamber filled with AHL using bent
339 tungsten pins.

340 The antennal lobe (AL) of the brain was located by morphology using an Olympus
341 BX51WI microscope and 40X/0.8NA objective. A FHC concentric bipolar electrode (CBAEB50)
342 was positioned in the center of the AL using a manual micromanipulator. During each
343 experimental trial, 4 electrical stimulus trains were delivered to the AL by an A.M.P.I. Master-8
344 pulse generator with a 20 second inter-train interval. The stimulus trains were 20 pulses with a
345 1ms pulse duration at a 100Hz pulse rate. The stimulus voltage was raised on each trial; 3, 5, 7,
346 and 9 volt trials were performed on each brain.

347 The GCaMP6f response of the *GH146* terminals in the LH was measured using a
348 Hammamatsu Orca-ER camera controlled by Micro-Manager. Images were acquired at a 300
349 ms frame interval. Stimulus delivery and image acquisition were synchronized using a National
350 Instruments USB-6212 DAQ and a custom MATLAB program. Brains were continuously
351 perfused with room temperature (20-22°C) AHL during the experiment. All brains responded to
352 the high voltage (9V) stimulus, no brains were excluded, and the stimulus electrode was not
353 repositioned after the experiment began.

354 Imaging data were analyzed using a custom MATLAB program. The program aligned the
355 image time series to correct drift using the Image Processing Toolbox. An analysis region of
356 interest (ROI) and background (BG) region were manually defined, the per-frame mean
357 fluorescence of the ROI and BG were calculated, and the BG corrected fluorescent time series
358 was calculated. The ΔF/F was calculated for each frame *i* using the formula: $\Delta F_i / F = (F_i - F_{1\text{-}20})$
359 $/ F_{1\text{-}20}$. The peak change in ΔF/F was calculated as the ΔF/F of the stimulus frame minus the
360 ΔF/F of the frame before the stimulus. The sustained level of ΔF/F was calculated as the mean
361 ΔF/F of frames 1-5 seconds after the stimulus minus the ΔF/F of the frame before the stimulus.
362 Frame time-stamps were used to generate a mean peri-stimulus ΔF/F of each trial. The timing
363 of each frame varied by several milliseconds due to software delays so, for display, the data
364 was re-sampled to a uniform 10 Hz time base using shape-preserving piecewise cubic
365 interpolation.

Modelling

Characterization of EAG channels. Time series data of currents in HEK cells expressing EAG channels during voltage clamp were used to characterize the activation functions and kinetics of EAG channels. Peak currents in HEK cells as a function of voltage were subtracted from peak currents in EAG-expressing HEK cells to isolate the currents due to EAG channels alone. Leak currents were then subtracted from this I-V curve, which was then converted to a curve of conductance *vs.* voltage using a reversal potential $E_K = -106.17$mV. EAG channels were modelled using the Hodgkin-Huxley framework (Hodgkin and Huxley 1952). The current due to EAG channels is given by

$$I_{EAG} = \bar{g}m(V - E)A$$

where $\bar{g}$ is the specific conductance of the channels, m is the activation variable, E is the reversal potential and A is the surface area of the compartment. m is a time varying variable determined by

$$\tau_m \frac{dm}{dt} = m_\infty - m$$

where m_∞ and τ_m are functions of the membrane potential V that are determined by fitting functions to plots of conductance *vs.* voltage and time-series of conductance at various holding voltages. Since the activity of EAG channels also depends on the intracellular calcium concentration, the process was repeated for multiple calcium concentrations to obtain functions that depended on both the membrane potential and the calcium concentration. For these channels, we used

$$m_\infty(V, Ca) = \left[\frac{0.0929}{0.0929 + [Ca^{2+}]}\right]\left[\frac{1}{1 + \exp\left(\frac{V + 23.12}{-16.94}\right)}\right]$$

for wild-type EAG channels and

$$m_\infty(V, Ca) = \left[\frac{0.8740}{0.97 + [Ca^{2+}]}\right]\left[\frac{1}{1 + \exp\left(\frac{V + 23.12}{-16.94}\right)}\right]$$

for CaMBD mutant EAG channels. Note that the mutant and wild-type channels differ in their calcium sensitivity, but not in their voltage sensitivity (Figure 1C). For both wild-type and mutant EAG channels, we found that the timescale of activation was not a strong function of calcium concentration; so we used

$$\tau_m(V) = 5497 - \frac{5500}{1 + \exp\left(\frac{V + 251.5}{-16.94 - 51.5}\right)}$$

395 In these functions, V is in units of mV, τ_m is in ms, and $[Ca^{2+}]$ is in μM.

396 *Model of presynaptic terminal.* Because EAG is inhibited only at relatively high levels of
397 intracellular calcium, we reasoned that a possible zone where EAG could be inhibited is the
398 micro domain close to voltage-gated calcium channels (VGCCs) at the presynaptic terminal. We
399 modelled the presynaptic terminal using a three-compartment model: one for the invading action
400 potential, another for the calcium micro-domain, and a third for parts of the pre-synaptic terminal
401 far from VGCCs. The calcium micro-domain had voltage-gated sodium channels, potassium
402 channels, EAG channels, and calcium channels. The other compartment had the same channel
403 profile, except for calcium channels. All compartments were electrically coupled to each other
404 with a conductance of 0.1 nS.

405 The activation functions and kinetics of sodium channels were determined using fits to
406 data from embryonic *Drosophila* neurons (O'Dowd and Aldrich 1988); potassium channels from
407 *Drosophila* photoreceptors (Hardie 1991) and calcium channels from *Drosophila* embryonic
408 muscles (Hara et al. 2015).

409 The model was integrated using the exponential Euler method (Dayan and Abbott 2001)
410 using a general-purpose neuron simulator written in C++, that we have made freely available at
411 https://github.com/sg-s/xolotl/.

412 *Code availability.* A script to reproduce Figure 5, a toolbox to interactively vary
413 parameters in the model, and scripts to estimate gating functions of EAG from raw data are
414 available at https://github.com/marderlab/eag .

415

416 **Learning and memory assays**

417 Appetitive conditioning protocol was as described previously (Liu et al., 2012). A group
418 of ~50 flies in a training tube alternatively received 10% 3-octanol (OCT; Merck) and 10% 4-
419 methylcyclohexanol (MCH; Sigma-Aldrich) for 1 min for immediate memory or for 2 min for 24 h
420 memory. Flies were loaded into CS+ tubes containing 2M dried sucrose filter papers with one
421 odor presentation and then CS- tubes without sucrose papers with the other odor. After a
422 certain retention time (2 min or 24 h), the trained flies were allowed to choose between OCT
423 and MCH for 2 min in the T-maze. A learning index was then calculated by taking the mean
424 performance indices (PIs) of the two reciprocally trained groups. Each PI was calculated by the
425 differences of flies choosing CS+ and CS- divided by the total number of flies. To control
426 whether the learning deficits were due to lack of sensation of sucrose or odors, flies were
427 allowed to choose between sucrose+ and sucrose- tubes for 2 min or between one odor (OCT

428 or MCH) and air for 2 min. Sucrose preference index or odor avoidance index was calculated,
429 respectively.
430
431 **Statistics**
432 *Electrophysiology:* Wilcoxon Rank Sum, unpaired Student's t-test and ANOVA done in
433 MATLAB (MathWorks, Natick, MA) or Excel (Microsoft).
434 *Memory:* statistical analyses were performed using GraphPad Prism 7. The Wilks-
435 Shapiro test was used to determine data normality. Normally distributed data were analyzed
436 with unpaired T-test, and data which did not pass the normality test were analyzed with a Mann-
437 Whitney test. Data are presented as mean ± SEM. Difference between groups were considered
438 significant at $p < 0.05$.
439
440 **Results**
441
442 ***Drosophila* EAG is inhibited by high $[Ca^{2+}]_i$**
443 Human EAG has three calmodulin (CaM) binding sites: one N-terminal and two C-
444 terminal (C1 and C2) (Ziechner et al. 2006) and is inhibited by nM levels of Ca^{2+} (Schonherr et
445 al. 2000). Previous work on *Drosophila* EAG, in which it was compared to hEAG1, suggested
446 that the fly channel was not regulated by Ca^{2+} (Schonherr et al. 2002). Intrigued by the fact that
447 all of these sites appear to be conserved in *Drosophila* (Figure 1A), we revisited the issue of
448 regulation by Ca^{2+} by expressing wildtype (WT) EAG, or a C-terminal CaMBD mutant form
449 (F732S,F735S, Sun et al. 2004), in HEK293 cells and recording currents with varying amounts
450 of Ca^{2+} in the pipette internal solution. Mutant and WT channels were expressed at comparable
451 levels (Figure 1B) and GFP was co-expressed to identify transfected cells.
452 As previously reported (Schonherr et al. 2002), *Drosophila* EAG was not inhibited at or
453 below 1 μM $[Ca^{2+}]_i$. Only when $[Ca^{2+}]_i$ was increased to high μM levels, did we see significant
454 inhibition. Figure 1C (left panel) shows currents recorded in the presence of 100 μM Ca^{2+}.
455 Currents from cells transfected with WT EAG are clearly reduced compared to those from cells
456 expressing EAG carrying mutations which block CaM-binding to the major C-terminal site. The
457 voltage-dependence of the channel is unaffected by this mutation (Figure 1C, right panel). The
458 dose-response relationship for $[Ca^{2+}]_I$ is shown in Figure 1D. WT EAG current density
459 approaches that of untransfected cells at high $[Ca^{2+}]_I$ while the CaMBD mutant has substantial
460 residual current even at mM levels of Ca^{2+} in the pipette.
461

462 **The C-terminal CaMBDs likely dominates Ca^{2+} sensitivity of EAG**

463 Examination of genomic data for the *eag* gene revealed that the N-terminal CaMBD,
464 which is a critical partner of the C-terminal site for Ca^{2+}-dependent gating (Whicher and
465 MacKinnon 2016), is located at an exonic junction that is alternatively spliced (Attrill et al. 2016,
466 Figure 1A). Since CaM is known to bind amphipathic helices, variation at this region is
467 potentially important for the affinity of CaM-binding and could potentially explain the published
468 Ca^{2+}-insensitivity of the canonical "WT" EAG (Drysdale et al. 1991a), which corresponds to the
469 PA splice variant curated on FlyBase, due to a dysfunctional N-terminal binding domain. The
470 splice site found in PA is also present in the PD and PG proteins, but the PE splice form has a 2
471 amino acid deletion, making it more like the mammalian EAG1 protein, while the PF variant has
472 an additional 7 amino acids inserted into the predicted amphipathic helix. To determine if splice
473 variation at this site alters the Ca^{2+}-sensitivity of EAG, we transfected each of the splice forms
474 into HEK293 cells and assayed their response to changes in [Ca^{2+}] (Figure 1E). Neither PE nor
475 PF were more sensitive to Ca^{2+} than the original PA isoform and all were significantly less
476 sensitive than mEAG1, which was completely inhibited at 500 nM $[Ca^{2+}]_i$. We conclude that the
477 functional sensitivity of *Drosophila* EAG to inhibition by Ca^{2+} is likely set by the C-terminal
478 CaMBDs since it is unchanged by variation in the N-terminal domain.
479

480 **Construction and characterization of a CaMBD mutant at the endogenous *eag* locus**

481 The low sensitivity of EAG to Ca^{2+}/CaM inhibition is notable. Bulk cytoplasmic Ca^{2+} is
482 modulated in the nM to low μM range in neurons. The HEK cell results show a partial gain-of-
483 function phenotype in the CaMBD mutant EAG channel due to inhibition at very high Ca^{2+} levels
484 (Figure 1D). The only cytoplasmic domains that have levels of Ca^{2+} (mM) that are this high are
485 near the mouth of open Ca^{2+} channels (Parekh 2008). The affinity of EAG for Ca^{2+}/CaM
486 suggests that it would only be inhibited if it were localized to this type of Ca^{2+} channel
487 microdomain *in vivo.*

488 To determine if there were a physiological role for Ca^{2+}-dependent inhibition of EAG, we
489 engineered the C-terminal CaMBD mutations characterized above into the endogenous *eag*
490 locus by ends-out homologous recombination (Figure 2A). Multiple alleles containing the
491 F732S,F735S mutations were recovered. WT strains, made in an identical manner with WT
492 recombination arms were also generated. Like the mutant alleles, these WT strains contain a
493 residual 76 bp loxP site located in an intron. These strains were used in all experiments as
494 controls due to their similar genetic background.

495 Biochemical analysis of adult head protein from CaMBD and WT flies by partial
496 purification on CaM-agarose and immunoblotting shows that EAG protein is present in
497 comparable amounts in both mutant and WT control alleles (Figure 2B, left panel). Quantitative
498 immunohistochemistry of larval brain neuropil (Figure 2B, right panel) confirms this. EAG is
499 normally present at high concentration in neuropil and can be seen in axons and at the
500 neuromuscular junction (NMJ) in larvae (see Sun et al. 2004 for immunohistochemistry of native
501 EAG) and the CaMBD mutation did not change this distribution (data not shown).
502
503 **Third instar NMJs in CaMBD mutants are morphologically normal and have no**
504 **spontaneous activity**
505 The NMJ of the third instar larva has been extensively used to assay excitatory synaptic
506 structure and function. *eag* null mutants have a characteristic constellation of phenotypes in this
507 preparation which include increases in the number of synaptic boutons (Budnik et al. 1990) and
508 a robust hyperexcitability phenotype in larval motor neurons seen both postsynaptically at
509 isolated NMJs (Drysdale et al. 1991b; Ganetzky and Wu 1983; Griffith et al. 1994) and at the
510 soma (Srinivasan et al. 2012). To determine if CaMBD mutants had morphological abnormalities
511 we stained third instar NMJs with antibodies to HRP and DLG to visualize presynaptic and
512 postsynaptic structures. NMJs from CaMBD and WT strains were indistinguishable (Figure 3A)
513 and there was no significant difference in bouton number.
514 We also performed current clamp recordings from muscle 6/7 to ask if the CaMBD
515 mutant was functionally normal. Baseline recordings from CaMBD and WT control animals
516 showed no significant level of spontaneous excitatory junctional potentials (EJPs, Figure 3B). In
517 contrast, recordings from NMJs of $eag^{\Delta Full}$, a molecular null mutant, had high levels of
518 spontaneous activity. In experiments in which we evoked release by nerve stimulation in normal
519 saline, we did not see any supernumerary EJPs in the CaMBD mutant (P.B., data not shown).
520
521 **CaMBD mutant third instar larvae exhibit decreases in the amplitude of evoked EJPs**
522 The EJPs seen in unstimulated *eag* null mutants are the result of spontaneous
523 depolarization of the presynaptic nerve terminal and synchronous Ca^{2+}-dependent release of
524 many vesicles. To determine if there were changes in spontaneous Ca^{2+}-independent release of
525 single vesicles, we recorded miniature excitatory junctional potentials (mEJPs). Neither the rate
526 nor the amplitude of this class of events was changed in CaMBD animals compared to WT
527 controls (mean mEJP frequency: WT12/8, 1.92 ± 0.21 Hz; CaMBD8/17, 1.46 ± 0.15 Hz, p =
528 0.09. Mean mEJP amplitude: WT12/8, 0.85 ± 0.04 mV; CaMBD8/17, 0.83 ± 0.05 mV, p = 0.8).

529 This indicates that the probability of release for individual vesicles and the quantal postsynaptic
530 response to glutamate are both unaffected by loss of regulation of EAG by Ca^{2+}.
531 We also assayed evoked release by stimulating the motor nerve with a suction pipette
532 and recording activity in the muscle. We saw a significant decrease in the amplitude of
533 stimulated EJPs in the CaMBD mutants and a reduced quantal content (Figure 3C). EAG is also
534 expressed in larval muscles (Zhong and Wu 1991; 1993), so to make sure that activation of the
535 EAG channels in the postsynaptic muscle did not confound the amplitude of potentials recorded
536 in the muscle, we voltage clamped the muscle and recorded excitatory junctional currents
537 (EJCs). As seen in Figure 3D, CaMBD mutants had significantly smaller EJC amplitudes than
538 controls. There was no significant difference in the decay of the CaMBD mutant EJCs compared
539 to WT controls (WT: 10.2 $\pm$ 0.5 ms, CaMBD mutant: 10.8 $\pm$ 1.8, $p = 0.8$, unpaired Student's T-
540 test.
541
542 **CaMBD domain mutants have reduced presynaptic Ca^{2+} influx**
543 The CaMBD mutant's reduction in quantal content and synaptic currents is consistent
544 with a gain of EAG function when Ca^{2+}/CaM is not able to inhibit EAG currents. As seen in
545 Figure 1C and D, the F732S,F735S mutation leads to larger EAG currents when internal Ca^{2+} is
546 at high concentrations. This could cause more effective repolarization of activated presynaptic
547 terminals and an early termination of Ca^{2+} influx, which would be predicted to decrease
548 neurotransmitter release. To test the effects of the mutation on Ca^{2+} influx directly, we
549 expressed GCaMP6 in olfactory projection neurons. These neurons have well-separated axonal
550 and dendritic processes that allow clear visualization of the presynaptic terminals in the lateral
551 horn. These neurons can be directly stimulated by applying current to the antennal lobes with a
552 bipolar stimulating electrode.
553 Figure 4 shows GCaMP responses in WT and CaMBD mutant terminals with different
554 levels of stimulation. Ca^{2+} influx increases with stimulation strength, with CaMBD mutant
555 sustained levels lower than WT at all voltages. Interestingly, the form of the WT Ca^{2+} response
556 changes at high stimulation levels. The peak appears to plateau and a shoulder appears that
557 increases the width of the response. These data are consistent with the effect of the CaMBD
558 mutant being a gain-of-function that terminates the Ca^{2+} influx from voltage-gated Ca^{2+}
559 channels.
560
561 **A simple model of the presynaptic terminal recapitulates changes in the width of action**
562 **potential and duration of the calcium influx**

563 The fact that Ca^{2+} influx appears to be blunted in the CaMBD mutant supports the idea
564 that this mutation produces a gain of function. However since the sensitivity of *Drosophila* EAG
565 to Ca^{2+} is very low, it is possible that it only matters if EAG is present close to areas of high local
566 Ca^{2+}. In presynaptic terminals, the voltage-gated Ca^{2+} channels that control neurotransmitter
567 release are highly localized to the active zone, a molecular complex where vesicle fusion occurs
568 (Kawasaki et al. 2004). In contrast, EAG immunohistochemistry (Gillespie and Hodge 2013; Sun
569 et al. 2004) suggests that EAG is widely distributed to areas where it would never see Ca^{2+}
570 levels high enough to cause inhibition. To determine if our electrophysiological and imaging
571 results were consistent with the presence of two distinct pools of EAG, one that could be
572 inhibited by Ca^{2+} and a second that was insensitive even in WT animals, we built a model of the
573 presynaptic terminal that contained pools of EAG that were both inside and outside of Ca^{2+}
574 microdomains (Figure 5). Using parameters obtained from our HEK cell experiments, we
575 determined that the behavior we observed at the NMJ and in adult brain could be obtained by
576 modeling EAG's behavior as compartment-specific. The model shows that both membrane
577 voltage and Ca^{2+} currents were regulated as predicted.
578
579 **Loss of Ca^{2+}-dependent inhibition of EAG increases somatic excitability**
580 While the decrease in presynaptic release at the NMJ appears to be due to a decrease
581 in excitability and Ca^{2+} influx, direct recordings from terminals are difficult, so we carried out
582 whole-cell patch clamp of identified MNISN-Is neurons in the ventral ganglion to more closely
583 examine the relationship between membrane potential and firing in the CaMBD mutant. Figure
584 6A shows representative traces of CaMBD and WT control neurons with increasing current
585 injection. CaMBD neurons fire earlier and at a higher rate than that WT controls. The complete
586 F/I curves are shown in Figure 6B. These data demonstrate that the CaMBD mutants are
587 somatically hyperexcitable.
588 Recordings were performed both in nominally Ca^{2+}-free external solution and in 1.8 mM
589 external Ca^{2+}. Interestingly, there was no difference with Ca^{2+} as a main effect between the two
590 sets of F/I curves (3-way ANOVA, $p = 0.9$). This indicates that it is unlikely that the Ca^{2+}-
591 dependent regulation of EAG normally plays a role in somatic excitability. This could either
592 mean that EAG is not present in the somatodendritic compartment, or that it is located too far
593 from sites of Ca^{2+} influx to be inhibited. Given previous literature on *eag* null mutants (Srinivasan
594 et al. 2012), it is more likely that this is an issue of differential localization.
595 The data from the soma present a significant contrast to those obtained at the NMJ,
596 where there appeared to be a pronounced hypoexcitabilty. Given that these results are from

597 different cellular compartments of the same motor neurons, it seem likely that there is
598 compartment-specific homeostatic compensation occurring that increases drive to motor neuron
599 terminals. The lack of effect of external Ca^{2+} suggests that the alterations in excitability do not
600 involve acutely Ca^{2+}-dependent processes. The increase in excitability may act to partially
601 compensate for the decrease in evoked amplitude.
602
603 **CaMBD mutants have memory defects**
604 The demonstration of a change in somatic excitability aimed at compensating for poor
605 presynaptic release suggested that homeostatic changes might be able to ameliorate the effects
606 of this mutation at the circuit level. To test this, we asked if associative memory, a complex
607 behavior with a well-described circuitry, was disrupted in the CaMBD mutant. Adult flies were
608 conditioned by presenting one odor in the presence of sugar, an appetitive stimulus, and a
609 different odor with no sugar. WT flies, when asked to choose between the two odors either
610 immediately (short-term memory) or 24 h after training (long-term memory) will choose the
611 paired odor significantly above chance. CaMBD mutants have impairment in both types of
612 memory (Figure 7A). Input behaviors, sugar preference and odor avoidance (Figure 7B) are not
613 impaired. If anything, the CaMBD mutants were better than the WT control lines for avoidance
614 of octanol. The level of short-term memory impairment was similar to that seen with *eag* null
615 mutants, which interestingly also have enhanced octanol avoidance (C.L., data not shown).
616 These data demonstrate that the dysregulation of excitability caused by the loss of Ca^{2+}
617 sensitivity of the EAG channel has widespread effects on neuronal circuits and disrupts complex
618 behaviors.
619
620 **Discussion**
621
622 An obvious role of protein localization is to limit the action of a molecule to a particular
623 cell compartment e.g. an anchored K^+ channel will only affect the membrane potential of a small
624 area surrounding it; a scaffolded kinase will preferentially phosphorylate substrates in the same
625 complex. Less obvious consequences of binding to a scaffold are alterations of the intrinsic
626 activities of the complexed molecules and generation of novel complex-specific effects on
627 neuronal processes. A well-known example of this is the fusion of vesicles carrying
628 neurotransmitters. Cytosolic bulk Ca^{2+} in neurons is typically regulated in the 10 nM to 10 μM
629 range and only cytoplasmic Ca^{2+} microdomains close to a voltage-dependent Ca^{2+} channel
630 (VDCC) ever see Ca^{2+} at mM concentrations. The SNARE machinery has very low Ca^{2+} affinity

631 and only functions when vesicles are docked to a complex with VDCCs (Stanley 2016). The
632 inhibition of *Drosophila* EAG channels by Ca^{2+} is likely to be facilitated by a similar type of
633 interaction. In this study we provide the first insights into its role by introducing mutations into
634 the endogenous *eag* locus that block regulation by Ca^{2+}.
635
636 ***Drosophila* EAG is inhibited by levels of Ca^{2+} only seen in VDCC microdomains**
637 The fly EAG channel had been thought to be an outlier with regard to regulation by Ca^{2+}.
638 In this study we show that it is regulated in the same manner as mammalian EAG1 (Figure 1).
639 The major difference between fly and mammalian EAGs appears to be sensitivity. Inhibition of
640 fly EAG is only see at high μM to mM Ca^{2+}. This is strikingly different from the regulation of
641 mammalian EAG1, which is fully inhibited at nM levels of Ca^{2+}. How the difference is sensitivity
642 is achieved in the fly protein is unknown, but we present evidence that the efficacy of regulation
643 of EAG channels by Ca^{2+}/CaM is controlled primarily by the C-terminal CaMBDs, as alternative
644 splicing in the fly gene at the site of the N-terminal CaMBD does not modulate apparent affinity.
645 This Ca^{2+}-dependent inhibition of EAG channels is a robust and evolutionarily conserved feature
646 of the channel family that has so far been without demonstrated function.
647
648 **Ca^{2+}-dependent inhibition of EAG may function to tune presynaptic release**
649 EAG channels are located in presynaptic terminals in both mammals and flies (Gillespie
650 and Hodge 2013; Mortensen et al. 2015) and characterization of knock outs suggest that it
651 participates in repolarization after action potential invasion (Wu et al. 1983). These loss of
652 function studies make it clear that repolarizing K^+ current is important for presynaptic function
653 and that the channel has a similar overall role across species. The role of Ca^{2+}-dependent
654 inhibition of EAG currents is not as well understood. The finding that evoked release was
655 decreased in the EAG CaMBD mutant in the face of normal spontaneous release dynamics and
656 quantal size argued that presynaptic EAG is normally exposed to very high levels of Ca^{2+} during
657 action potential-mediated neurotransmitter release, consistent with localization at active zones.
658 In mammals it has been speculated that the inhibition of EAG1 by Ca^{2+}/CaM serves as a
659 feedback mechanism to reduce the electrochemical driving force for Ca^{2+} influx (Schonherr et al.
660 2000). The idea is that EAG channels, if they were colocalized with VDCCs could control the
661 local membrane potential after an action potential during the time that the Ca^{2+} channels are
662 open. Inhibition of EAG by Ca^{2+} would allow the membrane potential to stay close the Ca^{2+}
663 reversal potential and blunt the electrochemical drive for Ca^{2+} influx through the open VDCC.
664 Our data (Figures 3 an 4) would argue against this hypothesis for the presynaptic terminal at the

665 larval NMJ since loss of regulation by Ca^{2+} decreases presynaptic release and evoked Ca^{2+}
666 influx. Whether this might be a viable mechanism for regulation of Ca^{2+} in dendrites would
667 require further investigation.
668 Another possible role for Ca^{2+}-dependent inhibition might be maintaining
669 neurotransmitter release during repetitive firing- essentially providing a way to turn down local
670 repolarization to maintain the ability to catalyze vesicle fusion. The dynamics of EAG inhibition
671 and its dependence of action potential pattern might provide clues to this aspect of EAG
672 function.
673
674 **Why is regulation by Ca^{2+} different in mammals and insects?**
675 The conservation of both N- and C-terminal CaMBDs from insects to mammals is
676 striking. Why would their apparent affinities be so disparate? The reason for the difference in
677 sensitivity between mammals and insects might have to do with how subcellular complexes are
678 constituted and the size of neurons and spines. The Ca^{2+}-sensitivity required to carry out a
679 function depends on the localization of the effector with respect to the Ca^{2+} source and the
680 nature of local Ca^{2+} buffering. Channels located in very close proximity to VDCCs do not require
681 high Ca^{2+} sensitivity, since they are exposed to very high (mM) local Ca^{2+} concentrations
682 (Tadross et al. 2013). Conversely, EAG channels that are inhibited with high affinity could be
683 affected by Ca^{2+} distant from the mouth of the VDCC. For fly neurons whose central processes
684 are very small, high affinity EAG inhibition might completely abolish all EAG current and render
685 neurons hyperexcitable. The Ca^{2+}-dependent inhibition of EAG could therefore contribute
686 maintaining presynaptic activity with repetitive stimulation in both species, but be tuned
687 differently due to differences in the location of the channels, buffering capacity of the neurons or
688 the size of the cell and synapse. A better understanding of the localizations of VDCCs and EAG
689 channels will be required to fully understand the role Ca^{2+}-dependent inhibition.
690
691 **The ion channel complexes are critical to nervous system function**
692 In neurons, ion channel-containing signaling complexes are a key class of protein
693 assemblage. The co-localization of proteins to the same complex can strongly influence the
694 kinetics and even the energetics of their activities and produce unforeseen interactions. Most of
695 a neuron's important biochemistry is not well-predicted by simply considering the equilibrium
696 state; Ca^{2+} microdomains are an excellent example of this principle. In this study, we present
697 data demonstrating that blocking the regulation of EAG by Ca^{2+} can disrupt the ability to form
698 memory (Figure 7). This argues that relatively subtle changes in the regulation of excitability can

699 have profound effects. There are an increasing number of examples of proteins whose function
700 requires their localization to a particular microdomain (Averaimo et al. 2016; Oheim et al. 2017;
701 Sanchez-Alonso et al. 2016). To understand how neurons work we must understand how
702 protein complexes shape signaling and the fly EAG channel will provide a useful model for this
703 endeavor.
704

705
706 ## Figure Legends

707

708 **Figure 1. *Drosophila* EAG channels are regulated by Ca^{2+}.** (A) Cartoon of the fly EAG
709 subunit showing the position of the highly conserved CaM binding domains (CaMBDs, not
710 drawn to scale). Protein sequence alignments of the three fly CaMBDs with human EAG as well
711 as comparison of the different *Drosophila* splice variants in the N-terminal CaMBD. Basic
712 residues are bold black, hydrophobic are bold gray. Arrows indicate the two phenylalanines
713 mutated to serines to disrupt CaM binding in the C2 domain. (B) Western blot of HEK293 cell
714 extracts expressing wild type (EAG-PA) or CaMBD (F232S,F235S) mutant plasmid DNA in
715 combination with an eGFP plasmid. (C) Sample traces of wild type or F232S,F235S mutant
716 EAG currents and I-V relation of EAG current densities recorded under whole-cell patch clamp
717 from HEK293 cells with 100 μM internal Ca^{2+} in pipette solution. (D) Plot comparing mean wild
718 type and CaMBD mutant EAG current densities at various internal Ca^{2+} concentrations at a
719 membrane voltage of 40 mV. Wild type (PA) and CaMBD mutant mean current densities are
720 significantly different at 100 and 500 μM internal Ca^{2+}, $p = 0.04$ for each concentration, Wilcoxon
721 rank sum test. (E) Plot of mean wild type EAG current densities for the N-terminal CaMBD
722 splice variants at 40 mV with mouse EAG for comparison. n represents number of cells
723 recorded. All values are mean ± SEM. There were no significant differences, $p = 0.4$, 2-factor
724 ANOVA between *Drosophila* splice isoforms across Ca^{2+} concentrations.

725

726 **Figure 2. Characterization of F232S,F235S CaMBD homologous recombination mutant**
727 ***Drosophila*.** (A) Schematic of the targeted region (exons 12-14) of the *Drosophila eag* locus
728 and the target vector used to generate the CaMBD mutants with F232S,F235S mutations. The
729 control line used the same target vector without the F232S,F235S mutations. (B) Western blot
730 (left) from a CaM bead pull-down of fly EAG from whole head extract of CaMBD mutant, WT
731 control and the $eag^{\Delta Full}$ null allele. The flow through and 2nd bead elutions were run to confirm all
732 of EAG was bound and released in the 1st elution. Flow through shows actin levels, indicating
733 loading was comparable for these samples. Larval brain immunohistochemistry (right) with EAG
734 antibody. Plot of the mean pixel intensity of the neuropil normalized to Actin immunostaining for
735 control and CaMBD mutant larvae. There is no significant difference in the normalized pixel
736 intensities for WT and CaMBD mutants, $p = 0.4$, unpaired Student's t-test. n represents number
737 of brains. Values are mean ± SEM.

738

739 **Figure 3. Characterization of the CaMBD mutant larval neuromuscular junction (NMJ).** (A)
740 Sample images from immunohistochemistry of WT and CaMBD mutant larval neuromuscular
741 junctions (muscles 6/7) with HRP and DLG antibodies to compare morphology of motor neuron
742 boutons. Plot of number of boutons at the muscle 6/7 NMJs for WT and CaMBD mutants. There
743 is no significant difference in the number of CaMBD mutant boutons compared to WT, $p = 0.6$,
744 unpaired Student's t-test. n represents number of NMJs from 4 larvae each for WT control and
745 CaMBD mutant. (B) Sample traces of spontaneous excitatory junctional potentials (EJPs) in
746 WT, CaMBD mutant and a molecular null of *eag* recorded in 0.4 mM external Ca^{2+}. Plot of the
747 mean spontaneous EJP frequencies. The CaMBD mutants are significantly different from the
748 *eag* full deletion, $p = 1.1 \times 10^{-7}$, Wilcoxon rank sum test. n represents number of cells from 5 WT
749 larvae, 6 CaMBD mutant larvae, and 7 full *eag* deletion larvae. (C) Sample traces of stimulated
750 EJPs and plot of mean quantal content in 0.2 mM external Ca^{2+}. The CaMBD mutants had a
751 significantly smaller quantal content, $p = 0.03$, Wilcoxon rank sum test. n represents number of
752 cells from 9 larvae for WT and 6 larvae for the CaMBD mutants. (D) Sample traces of stimulated
753 excitatory junctional currents (EJCs) and plot of mean EJC amplitudes recorded in 0.2 mM
754 external Ca^{2+} and normalized to muscle size. The mean current density of the CaMBD mutant
755 EJCs were significantly smaller than controls, $p = 4.7 \times 10^{-4}$, unpaired Student's t-test. n
756 represents number of larvae (1 cell recorded per larva). n.s. = not significant. Values are mean ±
757 SEM.
758
759 **Figure 4. CaMBD mutants have reduced evoked presynaptic Ca^{2+} influx** (A) Mean $\Delta F/F$ (%)
760 traces from imaging of GCaMP6 responses in the lateral horn axon terminals of *GH146-GAL4+*
761 neurons from adult brains before, during, and after electrical stimulation of the antennal lobe.
762 Shaded areas represent the $25^{th}/75^{th}$ percentile bounds. Arrow indicates time of stimulus (20 X 1
763 msec, 100 Hz). (B) Bar graphs of mean peak change in $\Delta F/F$ (top) and sustained level of $\Delta F/F$
764 (bottom) for each stimulus amplitude. With a 7 V stimulus, the mean peak change was
765 significantly lower in CaMBD mutants compared to controls, $p = 0.03$, and the sustained level
766 was significantly lower in CaMBD mutants at 7 V, $p = 0.004$, and 9V, $p = 0.001$; unpaired
767 Student's t-test with Bonferroni correction for multiple comparisons. n represents the number of
768 brains. Values are mean ± SEM.
769
770 **Figure 5. Action potential changes due to the CaMBD mutation in a simple model of the**
771 **presynaptic terminal.** (A) Schematic of the multi-compartment model of the presynaptic
772 terminal. The presynaptic terminal is modeled as 3 electrically coupled compartments: (1) the

773 invading action potential (gray box, top), (2) the Ca^{2+} microdomain with voltage-gated Ca^{2+}
774 channels and Ca^{2+} influx (black box), and (3) the parts of the synaptic terminal outside the Ca^{2+}
775 microdomain (dotted black box). (B) Evoked potentials in response to invading action potential
776 in the Ca^{2+} microdomain with WT EAG channels (black) and mutant EAG channels (gray). In
777 WT, EAG channels are inhibited by incoming Ca^{2+} and this generates a prolonged potential. The
778 CaMBD mutant EAG channels have reduced sensitivity to Ca^{2+} and the membrane potential
779 quickly repolarizes due to a gain of EAG function. (C) Comparison of evoked potentials in the
780 Ca^{2+} microdomain (solid black) and outside the Ca^{2+} microdomain (dotted). Since EAG channels
781 outside the micro-domain are not inhibited by incoming Ca^{2+}, they quickly repolarize the
782 membrane after an action potential. (D) Comparison of evoked Ca^{2+} influx with WT (black) and
783 CaMBD mutant EAG (gray). Similar to Figure 4, Ca^{2+} influx is larger and more prolonged in cells
784 with WT EAG than in cells with CaMBD mutant EAG. All parameters of the model are identical
785 between WT and mutant, and between the two compartments of the presynaptic terminal.
786
787 **Figure 6. Motor neurons show somatic hyperexcitability** (A) Sample traces of whole-cell
788 patch current clamp recordings from Type Is larval motor neuron cell bodies at selected current
789 stimulus steps (80 pA and 120 pA) in 0 mM or 1.8 mM external Ca^{2+}. (B) Spike frequency vs.
790 stimulus curves (F/I) for nominally Ca^{2+}-free and 1.8 mM external Ca^{2+}. There is no significant
791 difference in the mean spike frequencies with or without Ca^{2+}, $p = 0.9$, 3-factor ANOVA). The
792 CaMBD mutant mean spike frequencies were significantly higher than controls (0 mM Ca^{2+}: $p =$
793 3.1×10^{-5}; 1.8 mM Ca^{2+}: $p = 0.03$, 2-factor ANOVA). n represents number of motor neurons
794 recorded. Plotted values are mean ± SEM. All cells recorded in the 1.8 mM external Ca^{2+}
795 condition were first recorded in the nominally Ca^{2+}-free condition.
796
797 **Figure 7. Adult behavioral phenotypes of control and CaMBD mutant adults.** (A) Plot of the
798 performance index for 2 min and 24 h memory of CaMBD mutant 17.4.1 and WT control 12.6.1
799 adults in a *white*$^{+}$ genetic background. The CaMBD mutants had a significantly lower
800 performance index for appetitive conditioning, $p = 0.007$ for both 2 min and 24 h tests, 2-factor
801 ANOVA with Sidak's multiple comparison test. n represents the number of groups tested (see
802 methods). CaMBD mutant 8.8.1 showed a similar 2 min memory deficit, though 24 h memory
803 was not assayed (C.L., data not shown). (B) Quantification of sugar preference ($p = 0.4$) and
804 avoidance of 4-methylcyclohexanol (MCH, $p = 0.08$) and 3-octanol (OCT $p = 0.0002$). All values
805 are mean ± SEM and comparisons done with unpaired Student's T-test.
806

807 **References**

808

809 **Attrill H, Falls K, Goodman JL, Millburn GH, Antonazzo G, Rey AJ, Marygold SJ, and**
810 **FlyBase c**. FlyBase: establishing a Gene Group resource for Drosophila melanogaster. *Nucleic*
811 *Acids Res* 44: D786-792, 2016.

812 **Averaimo S, Assali A, Ros O, Couvet S, Zagar Y, Genescu I, Rebsam A, and Nicol X**. A
813 plasma membrane microdomain compartmentalizes ephrin-generated cAMP signals to prune
814 developing retinal axon arbors. *Nature communications* 7: 12896, 2016.

815 **Budnik V, Zhong Y, and Wu C-F**. Morphological plasticity of motor axons in *Drosophila*
816 mutants with altered excitability. *J Neurosci* 10: 3754-3768, 1990.

817 **Dayan P, and Abbott LF**. *Theoretical Neuroscience: Computational and mathematical*
818 *modeling of neural systems*. Cambridge, MA: MIT Press, 2001.

819 **Drysdale R, Warmke J, Kreber R, and Ganetzky B**. Molecular characterization of *eag*: A
820 gene affecting potassium channels in *Drosophila melanogaster*. *Genetics* 127: 497-505, 1991a.

821 **Drysdale R, Warmke J, Kreber R, and Ganetzky B**. Molecular characterization of eag: a gene
822 affecting potassium channels in Drosophila melanogaster. *Genetics* 127: 497-505, 1991b.

823 **Feng Y, Ueda A, and Wu CF**. A modified minimal hemolymph-like solution, HL3.1, for
824 physiological recordings at the neuromuscular junctions of normal and mutant Drosophila
825 larvae. *J Neurogenet* 18: 377-402, 2004.

826 **Ganetzky B, Robertson GA, Wilson GF, Trudeau MC, and Titus SA**. The eag family of K+
827 channels in Drosophila and mammals. *Ann N Y Acad Sci* 868: 356-369., 1999.

828 **Ganetzky B, and Wu CF**. Neurogenetic analysis of potassium currents in Drosophila:
829 synergistic effects on neuromuscular transmission in double mutants. *J Neurogenet* 1: 17-28,
830 1983.

831 **Gillespie JM, and Hodge JJ**. CASK regulates CaMKII autophosphorylation in neuronal growth,
832 calcium signaling, and learning. *Frontiers in molecular neuroscience* 6: 27, 2013.

833 **Griffith LC, Wang J, Zhong Y, Wu CF, and Greenspan RJ**. Calcium/calmodulin-dependent
834 protein kinase II and potassium channel subunit eag similarly affect plasticity in Drosophila. *Proc*
835 *Natl Acad Sci U S A* 91: 10044-10048, 1994.

836 **Gutman GA, Chandy KG, Adelman JP, Aiyar J, Bayliss DA, Clapham DE, Covarriubias M,**
837 **Desir GV, Furuichi K, Ganetzky B, Garcia ML, Grissmer S, Jan LY, Karschin A, Kim D,**
838 **Kuperschmidt S, Kurachi Y, Lazdunski M, Lesage F, Lester HA, McKinnon D, Nichols CG,**
839 **O'Kelly I, Robbins J, Robertson GA, Rudy B, Sanguinetti M, Seino S, Stuehmer W,**
840 **Tamkun MM, Vandenberg CA, Wei A, Wulff H, Wymore RS, and International Union of P**.
841 International Union of Pharmacology. XLI. Compendium of voltage-gated ion channels:
842 potassium channels. *Pharmacol Rev* 55: 583-586, 2003.

843 **Hara Y, Koganezawa M, and Yamamoto D**. The Dmca1D channel mediates Ca(2+) inward
844 currents in Drosophila embryonic muscles. *J Neurogenet* 29: 117-123, 2015.

845 **Hardie RC**. Voltage-sensitive potassium channels in Drosophila photoreceptors. *J Neurosci* 11:
846 3079-3095, 1991.

847 **Hodgkin AL, and Huxley AF**. A quantitative description of membrane current and its
848 application to conduction and excitation in nerve. *J Physiol* 117: 500-544, 1952.

849 **Kaplan W, Trout WE III**. The behavior of four neurological mutants of Drosophila. *Genetics* 61:
850 399-409, 1969.

851 **Kawasaki F, Zou B, Xu X, and Ordway RW**. Active zone localization of presynaptic calcium
852 channels encoded by the cacophony locus of Drosophila. *J Neurosci* 24: 282-285, 2004.

853 **Li Y, Liu X, Wu Y, Xu Z, Li H, Griffith LC, and Zhou Y**. Intracellular regions of the Eag
854 potassium channel play a critical role in generation of voltage-dependent currents. *J Biol Chem*
855 286: 1389-1399, 2011.

856 **Mortensen LS, Schmidt H, Farsi Z, Barrantes-Freer A, Rubio ME, Ufartes R, Eilers J,**
857 **Sakaba T, Stuhmer W, and Pardo LA**. KV 10.1 opposes activity-dependent increase in Ca2+
858 influx into the presynaptic terminal of the parallel fibre-Purkinje cell synapse. *J Physiol* 593: 181-
859 196, 2015.

860 **O'Dowd DK, and Aldrich RW**. Voltage-clamp analysis of sodium channels in wild-type and
861 mutant *Drosophila* neurons. *J Neurosci* 8: 3633-3643, 1988.

862 **Oheim M, Schmidt E, and Hirrlinger J**. Local energy on demand: Are 'spontaneous' astrocytic
863 Ca2+-microdomains the regulatory unit for astrocyte-neuron metabolic cooperation? *Brain Res*
864 *Bull* 2017.

865 **Parekh AB**. Ca2+ microdomains near plasma membrane Ca2+ channels: impact on cell
866 function. *J Physiol* 586: 3043-3054, 2008.

867 **Parks AL, Cook KR, Belvin M, Dompe NA, Fawcett R, Huppert K, Tan LR, Winter CG,**
868 **Bogart KP, Deal JE, Deal-Herr ME, Grant D, Marcinko M, Miyazaki WY, Robertson S, Shaw**
869 **KJ, Tabios M, Vysotskaia V, Zhao L, Andrade RS, Edgar KA, Howie E, Killpack K, Milash**
870 **B, Norton A, Thao D, Whittaker K, Winner MA, Friedman L, Margolis J, Singer MA,**
871 **Kopczynski C, Curtis D, Kaufman TC, Plowman GD, Duyk G, and Francis-Lang HL**.
872 Systematic generation of high-resolution deletion coverage of the Drosophila melanogaster
873 genome. *Nature genetics* 36: 288-292, 2004.

874 **Sanchez-Alonso JL, Bhargava A, O'Hara T, Glukhov AV, Schobesberger S, Bhogal N,**
875 **Sikkel MB, Mansfield C, Korchev YE, Lyon AR, Punjabi PP, Nikolaev VO, Trayanova NA,**
876 **and Gorelik J**. Microdomain-Specific Modulation of L-Type Calcium Channels Leads to
877 Triggered Ventricular Arrhythmia in Heart Failure. *Circ Res* 119: 944-955, 2016.

878 **Schonherr R, Gessner G, Lober K, and Heinemann SH**. Functional distinction of human
879 EAG1 and EAG2 potassium channels. *FEBS Lett* 514: 204-208, 2002.

880 **Schonherr R, Lober K, and Heinemann SH**. Inhibition of human ether a go-go potassium
881 channels by Ca(2+)/calmodulin. *Embo J* 19: 3263-3271., 2000.

882 **Srinivasan S, Lance K, and Levine RB**. Contribution of EAG to excitability and potassium
883 currents in Drosophila larval motoneurons. *J Neurophysiol* 107: 2660-2671, 2012.

884 **Staber CJ, Gell S, Jepson JE, and Reenan RA**. Perturbing A-to-I RNA editing using genetics
885 and homologous recombination. *Methods Mol Biol* 718: 41-73, 2011.

886 **Stanley EF**. The Nanophysiology of Fast Transmitter Release. *Trends Neurosci* 39: 183-197,
887 2016.

888 **Stansfeld CE, Roper J, Ludwig J, Weseloh RM, Marsh SJ, Brown DA, and Pongs O**.
889 Elevation of intracellular calcium by muscarinic receptor activation induces a block of voltage-
890 activated rat ether-a-go-go channels in a stably transfected cell line. *Proc Natl Acad Sci U S A*
891 93: 9910-9914, 1996.

892 **Sun XX, Hodge JJ, Zhou Y, Nguyen M, and Griffith LC**. The *eag* potassium channel binds
893 and locally activates calcium/calmodulin-dependent protein kinase II. *J Biol Chem* 279: 10206-
894 10214, 2004.

895 **Tadross MR, Tsien RW, and Yue DT**. Ca2+ channel nanodomains boost local Ca2+
896 amplitude. *Proc Natl Acad Sci U S A* 110: 15794-15799, 2013.

897 **Thibault ST, Singer MA, Miyazaki WY, Milash B, Dompe NA, Singh CM, Buchholz R,**
898 **Demsky M, Fawcett R, Francis-Lang HL, Ryner L, Cheung LM, Chong A, Erickson C,**
899 **Fisher WW, Greer K, Hartouni SR, Howie E, Jakkula L, Joo D, Killpack K, Laufer A,**
900 **Mazzotta J, Smith RD, Stevens LM, Stuber C, Tan LR, Ventura R, Woo A, Zakrajsek I,**
901 **Zhao L, Chen F, Swimmer C, Kopczynski C, Duyk G, Winberg ML, and Margolis J**. A
902 complementary transposon tool kit for Drosophila melanogaster using P and piggyBac. *Nature*
903 *genetics* 36: 283-287, 2004.

904 **Ufartes R, Schneider T, Mortensen LS, de Juan Romero C, Hentrich K, Knoetgen H,**
905 **Beilinson V, Moebius W, Tarabykin V, Alves F, Pardo LA, Rawlins JN, and Stuehmer W**.
906 Behavioural and functional characterization of Kv10.1 (Eag1) knockout mice. *Human molecular*
907 *genetics* 22: 2247-2262, 2013.

908 **Wang JW, Wong AM, Flores J, Vosshall LB, and Axel R**. Two-photon calcium imaging
909 reveals an odor-evoked map of activity in the fly brain. *Cell* 112: 271-282, 2003.

910 **Warmke JW, and Ganetzky B**. A family of potassium channel genes related to eag in
911 Drosophila and mammals. *Proc Natl Acad Sci U S A* 91: 3438-3442, 1994.

912 **Whicher JR, and MacKinnon R**. Structure of the voltage-gated K(+) channel Eag1 reveals an
913 alternative voltage sensing mechanism. *Science* 353: 664-669, 2016.

914 **Wu CF, Ganetzky B, Haugland FN, and Liu AX**. Potassium currents in *Drosophila:* different
915 components affected by mutations of two genes. *Science* 220: 1076-1078, 1983.

916 **Zhong Y, and Wu CF**. Alteration of four identified K+ currents in Drosophila muscle by
917 mutations in eag. *Science* 252: 1562-1564, 1991.

918 **Zhong Y, and Wu CF**. Modulation of different K+ currents in Drosophila: a hypothetical role for
919 the Eag subunit in multimeric K+ channels. *J Neurosci* 13: 4669-4679, 1993.

Ziechner U, Schonherr R, Born AK, Gavrilova-Ruch O, Glaser RW, Malesevic M, Kullertz G, and Heinemann SH. Inhibition of human ether a go-go potassium channels by Ca2+/calmodulin binding to the cytosolic N- and C-termini. *The FEBS journal* 273: 1074-1086, 2006.

Table 1. Conditions and cell properties for electrophysiological recordings

				RMP (mV)		Cm (pF)		Rm (GΩ)		Rs (MΩ)	
Cell Type	Genotype	# Cells	Ca^{2+}	Initial	Final	Initial	Final	Initial	Final	Initial	Final
Motor Neuron	WT	5	0 mM Ext.	-50.2±1.3	-47.6±2.9	23.5±0.4	21.9±0.3	0.91±0.1	1.01±0.1	35.0±4.3	43.4±8.7
Motor Neuron	CaMBD mut.	7	0 mM Ext	-56.3±1.5	-56.0±1.5	25.2±0.8	22.9±0.8	0.88±0.2	1.02±0.2	36.9±3.9	53.5±8.7
Motor Neuron	WT	3	1.8 mM Ext.	-48.0±1.5	-49.3±1.9	20.3±0.5	19.1±0.5	0.92±0.1	0.96±0.1	40.6±7.0	52.6±13.6
Motor Neuron	CaMBD mut.	4	1.8 mM Ext.	-55.3±2.2	-55.3±1.9	22.6±1.4	21.0±1.3	1.08±0.3	0.92±0.2	48.9±10.8	65.9±10.6
HEK	WT	13	13 nM Int.	-38.5±2.0	-41.9±3.0	16.2±2.7	15.5±2.8	1.13±0.3	0.88±0.2	8.3±1.1	10.2±1.8
HEK	CaMBD mut.	9	13 nM Int.	-37.2±2.0	-36.6±3.0	17.6±3.8	16.8±4.2	0.6±0.1	0.42±0.1	9.1±1.7	11.5±1.5
HEK	WT	4	100 nM Int.	-43.3±3.4	-37.3±4.3	17.3±3.1	16.5±3.3	1.09±0.4	0.43±0.1	4.9±0.4	7.5±1.2
HEK	CaMBD mut.	5	100 nM Int.	-45.6±1.7	-43.2±0.7	20.5±4.2	27.3±10.7	1.30±0.6	1.26±0.6	8.3±0.7	12.6±1.1
HEK	WT	6	10 μM Int.	-41.5±4.1	-37.7±5.0	19.7±2.5	19.3±2.9	0.69±0.1	0.86±0.2	10.8±3.8	13.9±5.1
HEK	CaMBD mut.	4	10 μM Int.	-37.8±5.9	-38.5±10.5	17.5±5.0	13.9±2.2	1.01±0.4	0.77±0.2	12.0±4.4	13.1±2.9
HEK	WT	7	100 μM Int.	-41.7±0.9	-28.9±4.8	14.6±2.6	14.2±2.7	1.23±0.3	0.95±0.2	8.5±1.8	15.4±3.2
HEK	CaMBD mut.	6	100 μM Int.	-40.7±3.0	-43.5±4.2	16.8±1.8	16.2±1.6	1.57±0.4	0.91±0.2	6.7±1.6	11.3±2.2
HEK	WT	9	500 μM Int.	-39.7±4.3	-18.2±4.3	21.1±3.1	15.2±2.8	0.85±0.2	0.70±0.2	11.0±4.0	8.3±1.3
HEK	CaMBD mut.	7	500 μM Int.	-43.6±2.1	-34.9±4.2	24.5±4.0	15.8±2.9	0.76±0.2	0.53±0.2	8.3±1.0	11.6±3.4
HEK	EAG-PA	4	10 nM Int.	-37.8±3.7	-35.5±3.5	25.3±7.6	23.6±7.1	0.41±0.2	0.38±0.1	14.7±3.6	16.4±3.6
HEK	EAG-PE	3	10 nM Int.	-36.7±3.3	-41.7±1.7	17.5±9.3	17.0±9.1	1.23±0.4	1.11±0.4	11.5±3.2	13.7±3.8
HEK	EAG-PF	2	10 nM Int.	-34.5±1.5	-28.5±1.5	18.7±5.9	20.2±7.9	0.20±.04	0.43±0.2	14.0±0.9	14.4±0.5
HEK	GFP	4	10 nM Int.	-16.8±5.4	-21.3±6.6	12.7±2.7	12.2±2.7	1.95±0.2	1.34±0.2	10.4±2.0	11.7±2.8
HEK	EAG-PA	5	500 nM Int.	-38.2±3.7	-35.5±3.5	14.9±2.0	14.2±2.1	1.17±0.3	0.75±0.1	9.6±0.7	18.3±5.5
HEK	EAG-PE	8	500 nM Int.	-36.8±1.3	-29.9±3.0	13.6±1.9	13.3±1.8	0.56±0.2	0.33±0.1	8.2±0.9	10.1±1.0
HEK	EAG-PF	5	500 nM Int.	-32.8±3.0	-27.8±2.7	18.0±3.5	17.5±3.4	1.0±0.5	0.53±0.2	6.7±0.3	7.9±0.6
HEK	EAG-PA	3	1 μM Int.	-48.3±3.9	-42.0±7.5	10.1±0.3	9.7±0.2	1.09±0.5	1.0±0.4	8.2±0.9	10.4±1.9
HEK	EAG-PE	4	1 μM Int.	-39.5±3.0	-36.0±2.1	16.4±3.7	16.0±3.8	0.60±0.3	0.59±0.3	10.7±1.3	13.5±1.7
HEK	EAG-PF	4	1 μM Int.	-40.0±6.1	-26.5±6.6	19.6±5.8	18.7±5.4	0.67±0.4	0.85±0.6	13.4±2.7	16.6±3.3
HEK	GFP	3	1 μM Int.	-24.7±4.9	-18.3±6.2	12.2±2.0	11.5±2.2	1.02±.03	1.0±0.1	7.5±1.5	18.1±7.7
Muscle (VC)	WT	28	0.2 mM Ext.	-46.6±1.5		4.4±0.2 (nF)		0.0038 ±0.0003		0.14 ±0.0009	
Muscle (VC)	CaMBD mut.	30	0.2 mM Ext.	-46.8±1.1		4.8±0.1 (nF)		0.0027 ±0.0003		0.14 ±0.0009	

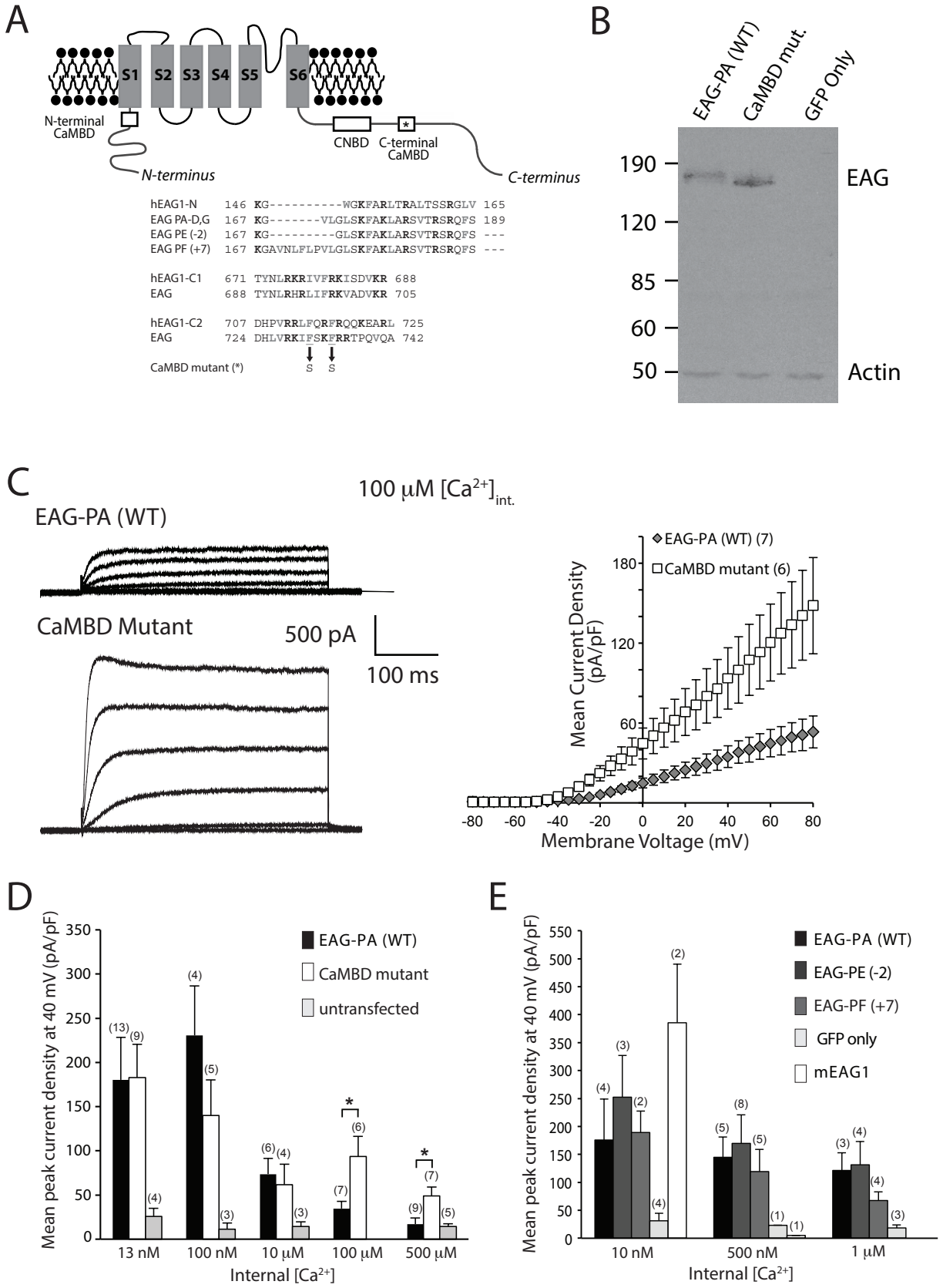
A
S1
S2
S3
S4
S5
S6
N-terminal CaMBD
CNBD
C-terminal CaMBD
N-terminus
C-terminus
hEAG1-N 146 KG----------WGKFARLTRALTSSRGLV 165
EAG PA-D,G 167 KG-------VLGLSKFAKLARSVTRSRQFS 189
EAG PE (-2) 167 KG---------GLSKFAKLARSVTRSRQFS ---
EAG PF (+7) 167 KGAVNLFLPVLGLSKFAKLARSVTRSRQFS ---
hEAG1-C1 671 TYNLRKRIVFRKISDVKR 688
EAG 688 TYNLRHRLIFRKVADVKR 705
hEAG1-C2 707 DHPVRRLFQRFRQQKEARL 725
EAG 724 DHLVRKIFSKFRRTPQVQA 742
CaMBD mutant (*) S S
B
EAG-PA (WT)
CaMBD mut.
GFP Only
190
120
85
60
50
EAG
Actin
C
100 μM [Ca2+]int.
EAG-PA (WT)
CaMBD Mutant
500 pA
100 ms
EAG-PA (WT) (7)
CaMBD mutant (6)
Mean Current Density (pA/pF)
Membrane Voltage (mV)
D
Mean peak current density at 40 mV (pA/pF)
EAG-PA (WT)
CaMBD mutant
untransfected
13 nM
100 nM
10 μM
100 μM
500 μM
Internal [Ca2+]
E
Mean peak current density at 40 mV (pA/pF)
EAG-PA (WT)
EAG-PE (-2)
EAG-PF (+7)
GFP only
mEAG1
10 nM
500 nM
1 μM
Internal [Ca2+]

Figure 1

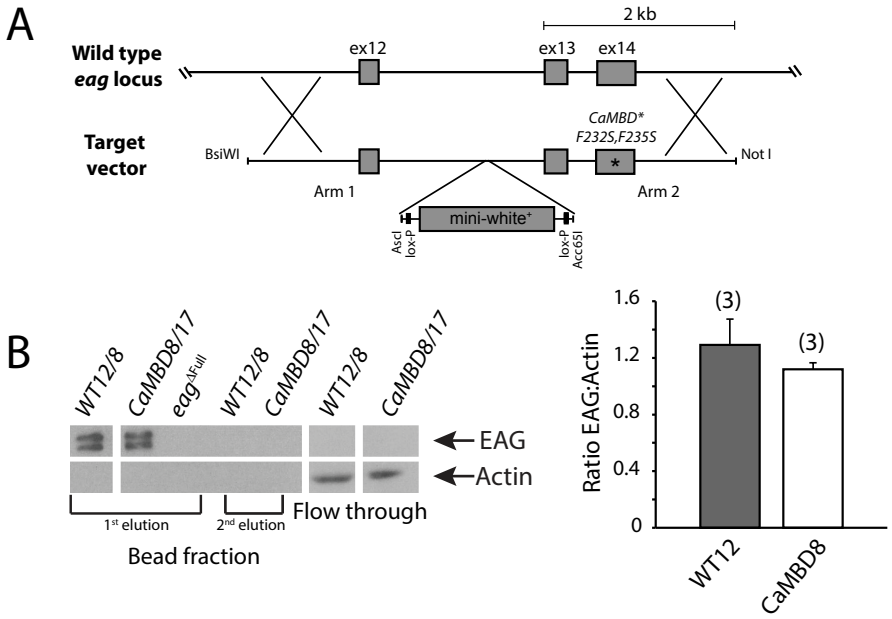
A
2 kb
Wild type
eag locus
ex12
ex13
ex14
Target
vector
BsiWI
CaMBD*
F232S,F235S
Not I
Arm 1
Arm 2
mini-white+
AscI
lox-P
lox-P
Acc65I
B
WT12/8
CaMBD8/17
eag Δ5'full
WT12/8
CaMBD8/17
WT12/8
CaMBD8/17
EAG
Actin
1st elution
2nd elution
Flow through
Bead fraction
Ratio EAG:Actin
1.6
1.2
0.8
0.4
0
(3)
(3)
WT12
CaMBD8

Figure 2

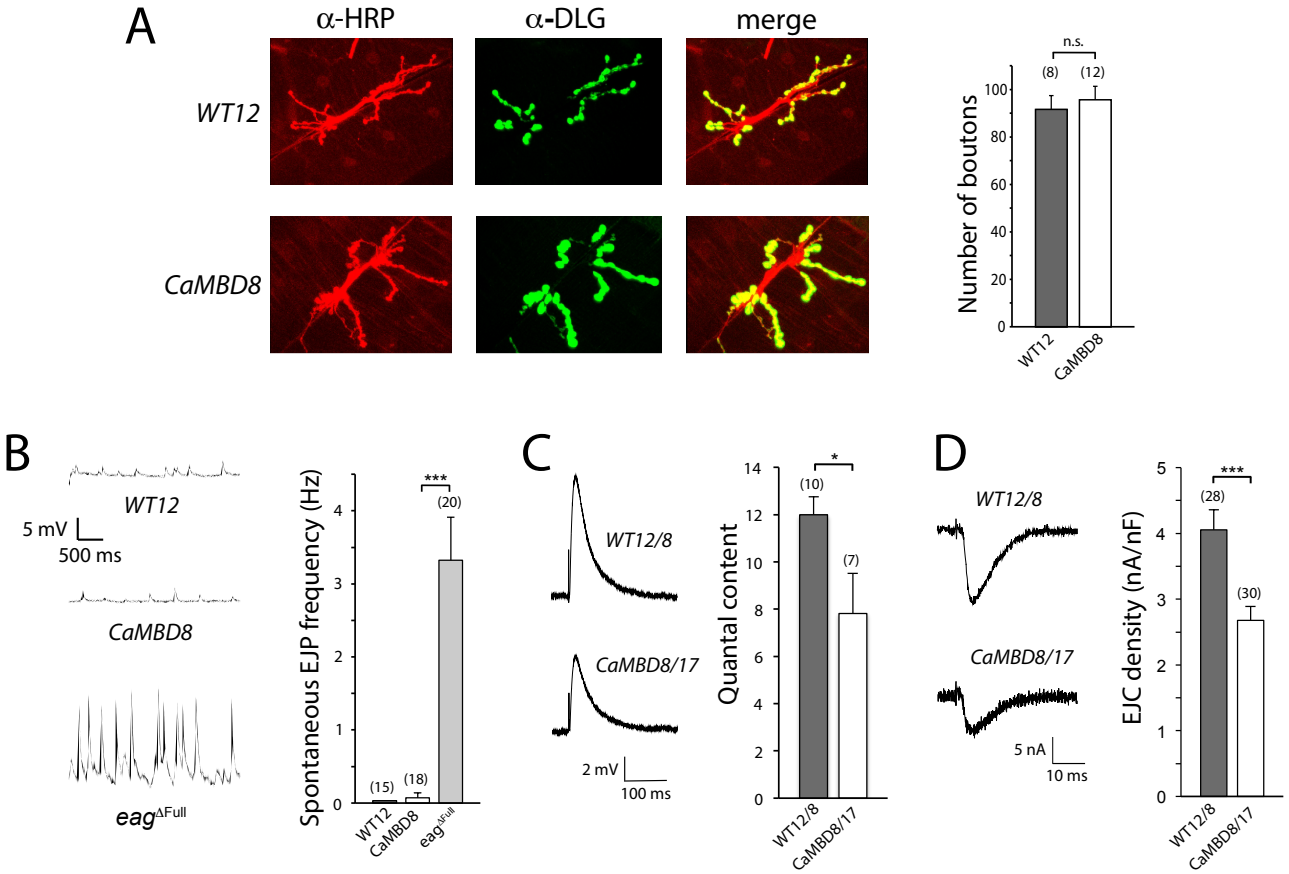
A
α-HRP
α-DLG
merge
WT12
CaMBD8
n.s.
(8)
(12)
Number of boutons
100
80
60
40
20
0
WT12
CaMBD8
B
WT12
5 mV
500 ms
CaMBD8
eag^ΔFull
Spontaneous EJP frequency (Hz)
***
(20)
(15)
(18)
4
3
2
1
0
WT12
CaMBD8
eag^ΔFull
C
WT12/8
CaMBD8/17
2 mV
100 ms
Quantal content
*
(10)
(7)
14
12
10
8
6
4
2
0
WT12/8
CaMBD8/17
D
WT12/8
CaMBD8/17
5 nA
10 ms
EJC density (nA/nF)
***
(28)
(30)
5
4
3
2
1
0
WT12/8
CaMBD8/17

Figure 3

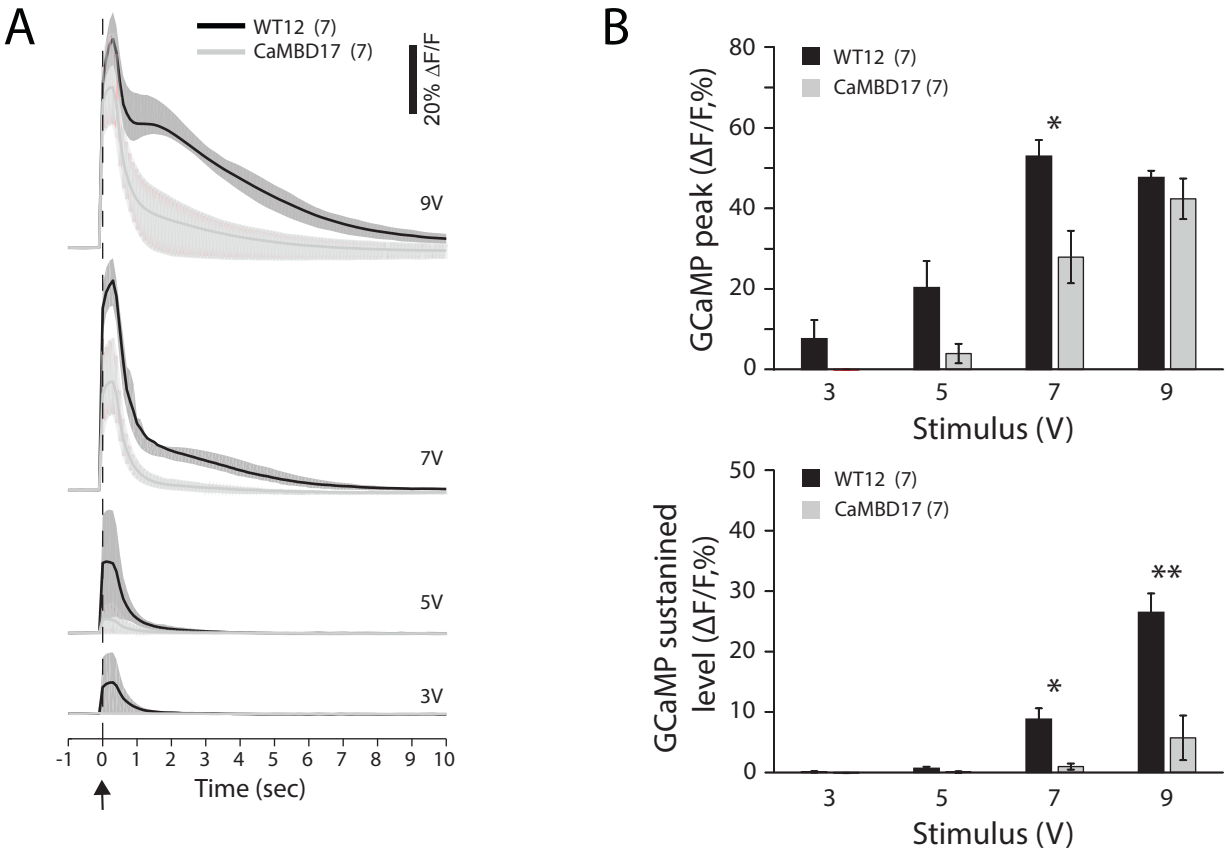
A
WT12 (7)
CaMBD17 (7)
20% ΔF/F
9V
7V
5V
3V
-1 0 1 2 3 4 5 6 7 8 9 10
Time (sec)
B
WT12 (7)
CaMBD17 (7)
GCaMP peak (ΔF/F,%)
80
60
40
20
0
*
3 5 7 9
Stimulus (V)
WT12 (7)
CaMBD17 (7)
GCaMP sustanined level (ΔF/F,%)
50
40
30
20
10
0
*
**
3 5 7 9
Stimulus (V)

Figure 4

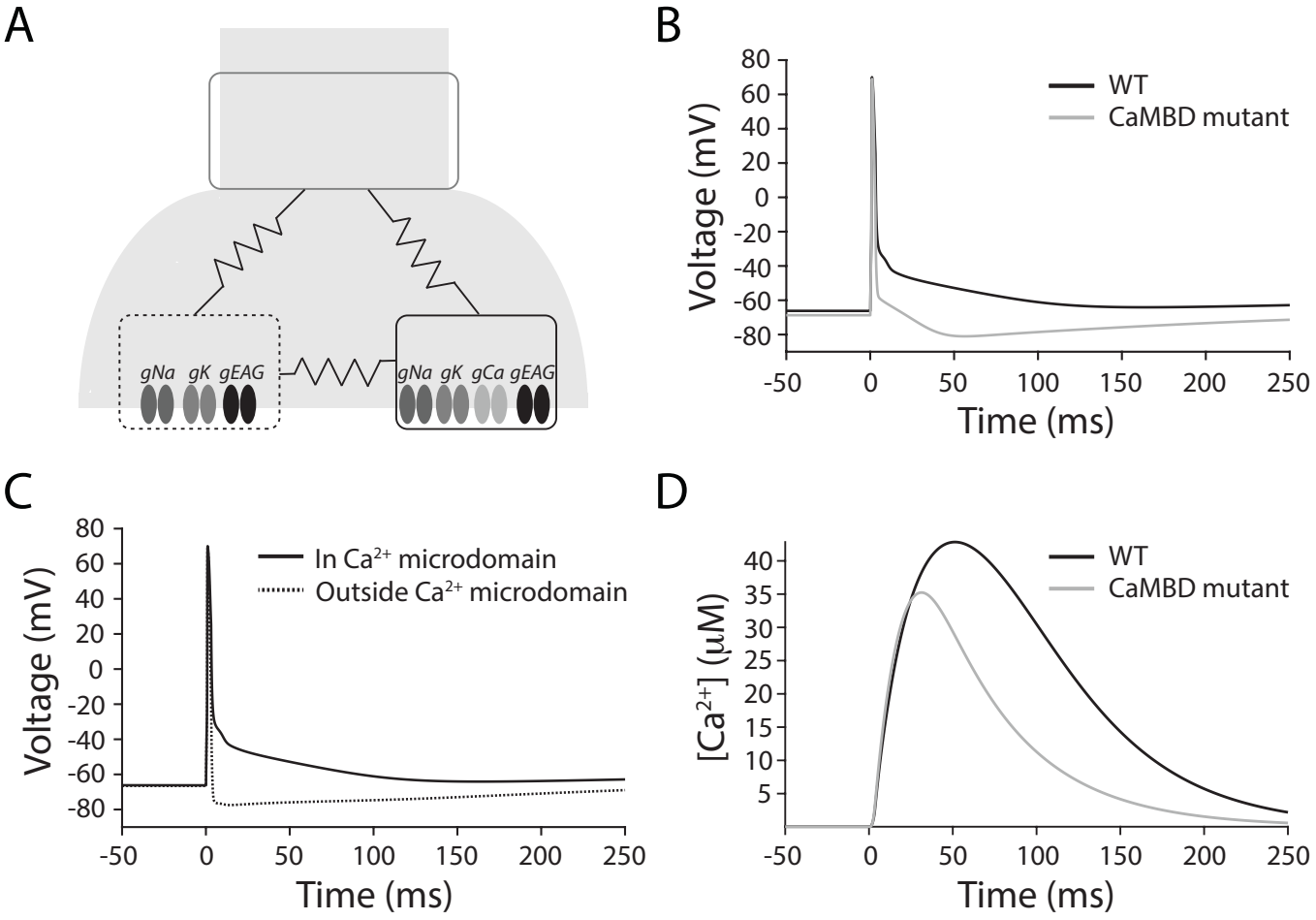
A
gNa gK gEAG
gNa gK gCa gEAG
B
WT
CaMBD mutant
Voltage (mV)
Time (ms)
C
In Ca2+ microdomain
Outside Ca2+ microdomain
Voltage (mV)
Time (ms)
D
WT
CaMBD mutant
[Ca2+] (μM)
Time (ms)

Figure 5

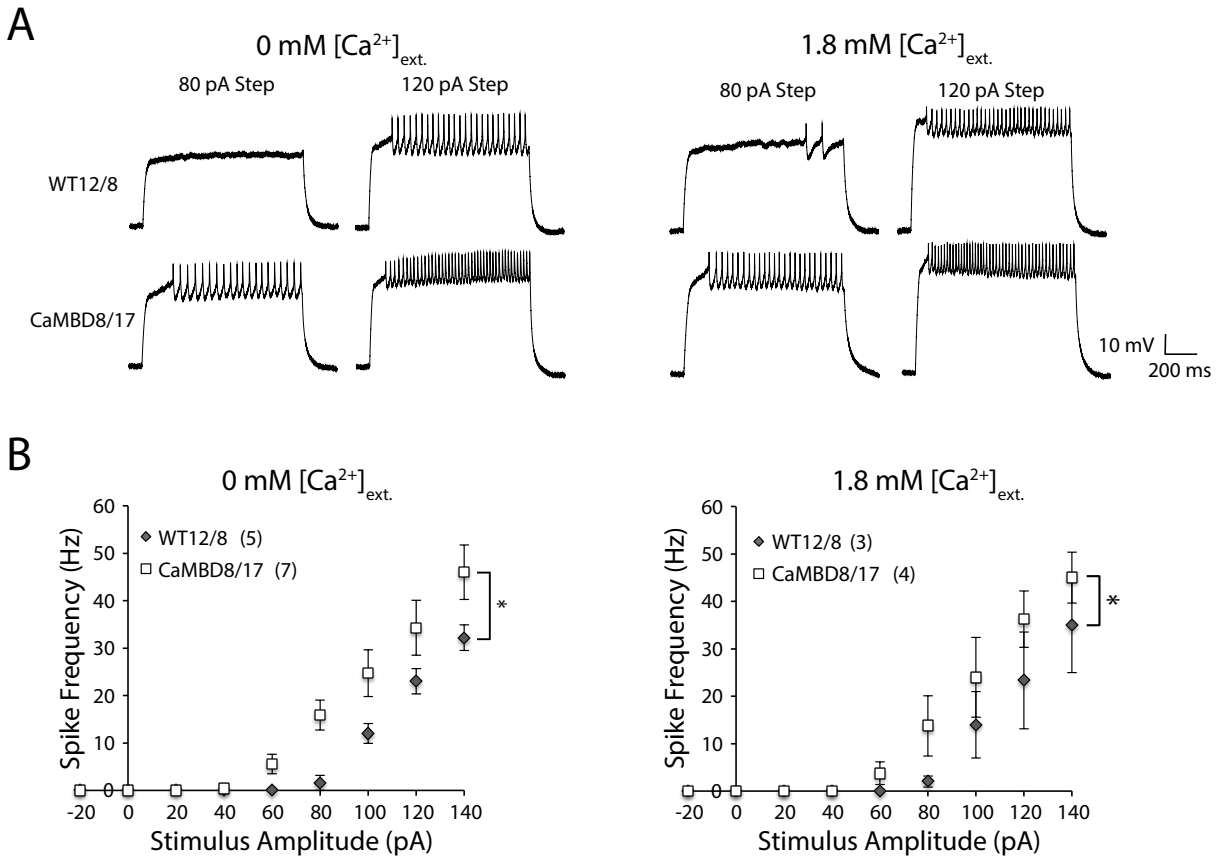
A
0 mM [Ca2+]ext.
1.8 mM [Ca2+]ext.
80 pA Step
120 pA Step
80 pA Step
120 pA Step
WT12/8
CaMBD8/17
10 mV
200 ms
B
0 mM [Ca2+]ext.
1.8 mM [Ca2+]ext.
WT12/8 (5)
CaMBD8/17 (7)
WT12/8 (3)
CaMBD8/17 (4)
Spike Frequency (Hz)
Stimulus Amplitude (pA)
*
*

Figure 6

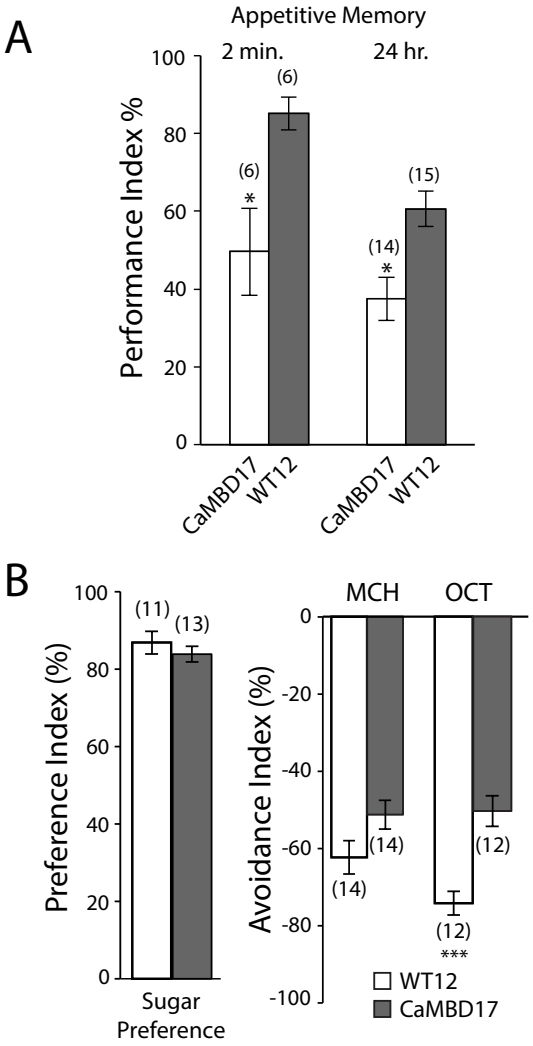
A
Appetitive Memory
2 min.
24 hr.
Performance Index %
100
80
60
40
20
0
(6)
(6)
*
(15)
(14)
*
CaMBD17
WT12
CaMBD17
WT12
B
Preference Index (%)
100
80
60
40
20
0
(11)
(13)
Sugar
Preference
MCH
OCT
Avoidance Index (%)
0
-20
-40
-60
-80
-100
(14)
(14)
(12)
(12)
***
WT12
CaMBD17

Figure 7